

A practical fabrication strategy for wire arc additive manufacturing of metallic parts with wire structures

Ziping Yu (✉ zy755@uowmail.edu.au)

University of Wollongong <https://orcid.org/0000-0002-2427-1433>

Zengxi Pan

University of Wollongong

Donghong Ding

Foshan University

Joseph Polden

University of Wollongong

Lei Yuan

University of Wollongong

Fengyang He

University of Wollongong

Huijun Li

University of Wollongong

Research Article

Keywords:

Posted Date: February 25th, 2021

DOI: <https://doi.org/10.21203/rs.3.rs-225836/v1>

License:  This work is licensed under a Creative Commons Attribution 4.0 International License.

[Read Full License](#)

A practical fabrication strategy for wire arc additive manufacturing of metallic parts with wire structures

Ziping Yu^a, Zengxi Pan^{a,*}, Donghong Ding^b, Joseph Polden^a, Lei Yuan^a, Fengyang He^a, Huijun Li^a

^a *School of Mechanical, Materials & Mechatronic, Faculty of Engineering and Information Sciences, University of Wollongong, Northfield Ave, Wollongong, NSW 2500, Australia*

^b *School of Mechatronic Engineering and Automation, Foshan University, Foshan, Guangdong 528225, China*

* *Corresponding author. E-mail zengxi@uow.edu.au*

Abstract

Wire Arc Additive Manufacturing (WAAM) is well suited for the manufacture of sizeable metallic workpieces featuring medium-to-high geometrical complexity due to its high deposition rate, low processing conditions limit, and environmental friendliness. To enhance the current capability of the WAAM process for fabricating structures with complex geometry, this paper proposes a robot-based WAAM strategy adapted specifically for fabricating free-form parts with wire structures composed of multiple struts. Contributions in this work include: (i) The study of bead modelling, which establishes optimal welding parameter selection for the process; (ii) The novel manufacturing strategy, including the adaptive slicing methodology and height control system for accurately depositing every single strut; (iii) Detailed manufacturing procedures for multi-strut branch intersections as well as the collision-free path planning to control the overall fabrication process. To verify the effectiveness of this proposed WAAM approach, two complex wire structures were fabricated successfully, indicating the feasibility of the proposed fabrication strategy.

Keywords

Additive manufacturing; Gas metal arc welding; Wire structures; Freeform fabrication

1. Introduction

Wire arc additive manufacturing (WAAM) is an emerging directed energy deposition additive

manufacturing technology [1] that utilizes electric arc as the power source, which can provide high heat input and deposition rates. Due to its rapid prototyping capability [2] and simplistic equipment setup [3, 4], it becomes a promising alternative to manufacture sizeable metallic components featuring medium-to-high geometrical complexity [5], particularly in aerospace, automotive, and rapid tooling industries [6].

In recent years, WAAM has been integrated with industrial robotic systems or computer-aided manufacturing (CAM) systems, allowing it to perform multi-axis freeform deposition in three-dimensional space [7], such as wire structures fabricated in ref [8]. Wire structures are skeleton-like components composed of many interconnected support struts. Initially, this type of structure has been widely employed in polymer AM. Huang et al. [9] pointed out that wire structures can reduce material requirements and costs if properly integrated into a given parts' design. Mueller et al. [10] stated that this structure could reduce the mass of a given component while maintaining its structural stability, thereby increasing the efficiency of the fabricating process. Similarly, for metallic wire structures, several attempts have been made to illustrate that using metal wire structures to replace thin-walled or solid structures enables weight reduction while maintaining high strength also [11]. Moreover, the MX3D team [12] carried out many high-profile projects that emphasize the unique artistic and practical values of these metal wire-structures.

A significant difference between the fabrication of wire structures and others (such as thin-walled or solid structures) is that the material is successively added in a point-by-point manner [8] instead of continuous bead deposition layer-by-layer [13]. Therefore, to successfully implement WAAM for producing wire structures, an accurate point-by-point bead model is required to predict and control the forming shape of each deposition and, ultimately, the geometry of the final part [14].

The adaptive slicing algorithm and multi-directional path planning method are also essential for the freeform fabrication of wire structures. Yuan et al. [15] have implemented a multi-directional deposition method for fabricating overhang parts without using any supports. Non-layerwise slicing methods are widely developed in AM of complex structures [16]. For the deposition strategy of the wire structures, Radel et al. [8] reported that struts could be fabricated through depositing material point-by-point in space with acceptable fabrication efficiency.

In producing wire structures, the welding torch may have a greater collision probability due to the

complexity of parts. Wu et al. [17] changed the orientation of the extrusion head to avoid the collision. However, in the WAAM of wire structures, the orientation of the welding torch is limited due to the characteristics of the welding process.

In this paper, a number of essential strategies for manufacturing metallic wire structures using the point-to-point WAAM process, from bead modelling to the final torch-based deposition path planning, were proposed. The developed methods aim to reduce manufacturing difficulty as well as enhance the overall efficiency in manufacturing these wire structures. The contributions here are demonstrated by fabricating two different parts with wire structures via the proposed methodology.

2. Problem Definitions

2.1 Wire structure definition

The parts with wire structures consist of a network of interconnected struts. Each strut is built up by a series of overlapping deposits formed layer-by-layer through spot welding, where the welding torch remains stationary. The projected shape of the deposits is similar to a hemisphere, as summarized by Abe et al. [19]. The characteristic geometric parameters of the deposits are defined by layer height-increment (Δh) and layer diameter (d), as shown in Fig. 1. Due to overlapping between neighboring beads, as described by Ding et al. [20], height-increment Δh of each layer is obtained by calculating the difference between the height of the next layer and the current layer, which is expressed as:

$$\Delta h_n = h_{n+1} - h_n \quad (1)$$

where n represents the number-of-time spot welding, this clarifies that the welding position of each layer is the same as the previous layer height coordinates. To highlight this, each layer of a strut is denoted as L_n , whose coordinates are the same as h_{n-1} . Whenever L_n is mentioned, it also includes a Δh_n , which is used to find the next welding layer L_{n+1} .

In the fabrication process, each layer is considered to have the same material composition and thermal conductivity. Note that the material of the substrate and the filled wire may have a subtle difference leading the inaccuracies in the process during the deposition of the first few layers. Thus, strut-like substrates consisting of several layers need to be deposited before starting to fabricate wire structures.

Due to unavoidable interferences in the physical welding process, layers with abnormal shapes may

occasionally appear, as shown in Fig. 1. For the experiments conducted in this work, these samples (which lie significantly outside of the average data range) will be excluded to reduce errors and improve the model accuracy.

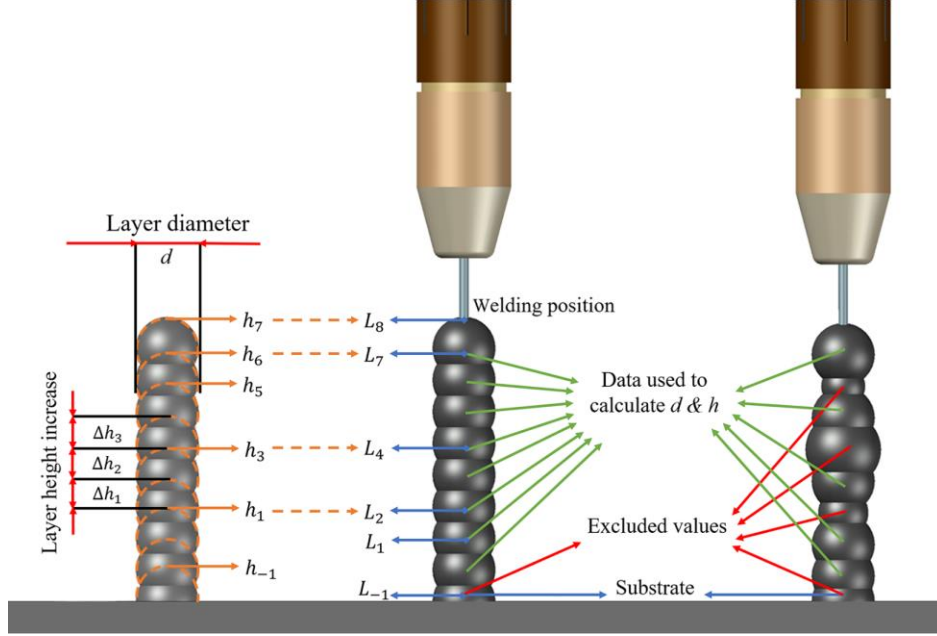


Fig. 1 Definition of layer geometry, substrate, and layer data collected.

2.2 Introduction to strut processing directions

A schematic diagram describing the build direction and torch direction of a wire structure is shown in Fig. 2. During the deposition, the torch direction always remains parallel with the build direction of the strut. During each welding period, the torch tip remains stationary at a certain distance above the welding point, referred as the contact to work distance (*ctwd*). A strut with an inclined build direction will feature a certain slope k between the two layers L_n and L_{n-1} . The direction of the welding torch also has an incline angle α_n (relative to the ground), defined as:

$$\alpha_n = \tan^{-1} \frac{L_{nz} - L_{n-1z}}{L_{nx} - L_{n-1x}} = \tan^{-1} k_n \quad (2)$$

It is worth noting that for these non-vertical struts, Δh is not measured vertically upward along the z-axis direction but follows the build direction of the strut with the slope k_{n+1} .

The alteration point highlighted in Fig. 2 is used to distinguish when the build direction of the strut varied so that the torch can adjust its direction accordingly. In situations where the build direction

changes smoothly with the Bezier curve, no alteration point is required. The geometric data required for these calculations can be readily obtained from CAD data. This point defined zones where an adaptive slicing process is required, which is detailed in the next sections.

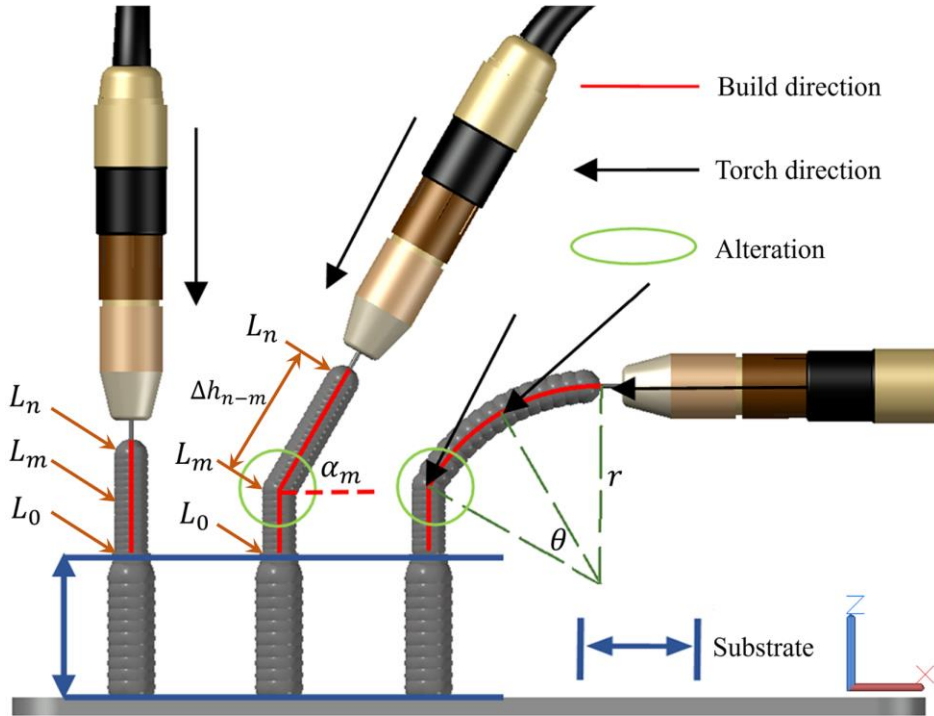


Fig. 2 The schematic of the build direction, torch direction of the single strut.

3. Experimental setup

Experiments were carried out employing the robotic WAAM system, as shown in Fig. 3, which includes an ABB IRB2600, the Fronius welding devices and welding system, and a 2 DOF workpiece positioner. The proposed WAAM system was controlled through an integrated computer-aided interface, presented previously in [14]. This software aimed to display arbitrary imported CAD models visually and obtain the desired workpiece geometry. It was designed to automatically slice the workpiece, calculate tool processing paths, and then directly generate the corresponding robot code and welding parameters for the manufacturing process.

A multi-functional tool was developed through integrating a CCD camera, a 3D profile scanner, and an infrared temperature sensor into a Fronius robacta drive CMT welding torch. The camera is used to capture the visual appearance of the workpiece during processing. A 3D profile scanner is used to obtain the geometric profile (layer height-increment and layer diameter) of deposited weld beads. The infrared temperature sensor is implemented to monitor the inter-layer temperature of the welding

process. The functions mentioned above, together with welding current and voltage acquisition functions, have been integrated into LabVIEW to establish a feedback control for improving the reliability and accuracy of the deposition process.

The filling wire was mild steel (ER70S-6) welding wire with a diameter of 0.9mm. A shielding gas mixture of 15% CO₂ and 85% argon was employed with a flow rate of 15 L/min. The chemical composition and mechanical properties of the selected welding wire are listed in **Table I**.

Table I Chemical composition and properties of ER70S-6

Chemical composition (wt.%)						
Composition	Mn	Si	Cu	C	S	P
ER70S-6 Wire	1.53	0.88	0.18	0.08	0.01	0.009

Properties in Specshield 15% CO₂, Ar

Melt temperature (T)	1700K
Density (ρ)	6500 kg/m ³
Surface tension (γ)	1.3 N/m
Tensile Strength	85-90,000 psi
Yield Strength	70-75,000 psi

The cold metal transfer (CMT) was adopted in the experiments aim to reduce the heat input during the deposition process with high-quality results. This method is substantially suitable for welding thin-walled structures with small widths [18], and here it also has the fabulous performance for depositing strut layers type.

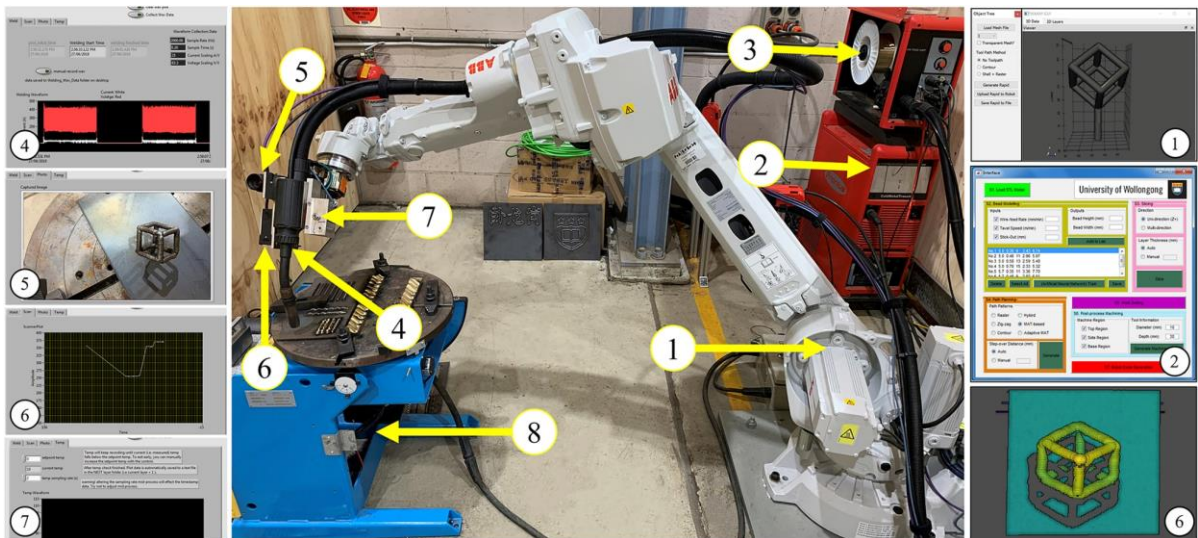


Fig. 3 WAAM system. (1) IRB 2600; (2) TransPuls Synergic 5000 CMT welder; (3) VR 7000 CMT wire feeder; (4) CMT torch; (5) CCD camera; (6) 3D profile scanner; (7) Infrared temperature sensor; (8) 2-DOF workpiece

positioner.

4. Implementation and discussion

The core contributions of this paper are presented here, which spread over four key areas: the strut-based bead modelling, a height control system, an adaptive slicing methodology, and finally, the tool path planning strategies that combine these techniques to produce an efficient means of fabricating complex wire structures.

4.1 Strut-based bead modelling

Process parameters have significant effects on the forming quality of the strut. Therefore, it is critical to establish a bead model suitable for the strut to determine the appropriate parameters for producing a geometrically accurate part. In this experiment, the welding arc-on time (wt) and wire feeding speed (wfs) are the primary process parameters that dominate the geometry formation of the strut. Across all tests, the inter-layer temperature is cooled down to around room temperature so as to ensure that each layer has the same heat condition. The $ctwd$ is maintained at 9mm to provide a relatively constant rate of gas shielding.

Experiments were conducted for four different wfs (from 4 to 7m/min) at four different wt (from 1.5 to 3s), as shown in **Table II**. Substrates with ten layers were first deposited with $wfs = 9\text{m/min}$ and $wt = 3\text{s}$ before the strut welding process began so as to eliminate the interference of external factors in the first few layers of struts. Each deposited strut consists of 20 layers, and two struts with the same set of process parameters were fabricated, so a total of 40 sets of data was obtained under each parameter combination, and the averaged forming results of these data are recorded as the final measured results.

Fig. 4 illustrates the effect of (a) wfs and (b) wt on the layer geometry. The graphs indicate a linear correlation between them and the change in Δh_m is more closely related to the value of wt . Based on this, a nonlinear regression equation is computed to correlate the resultant strut geometries relative to the wfs and wt , as shown in Fig. 4 (c). Their expressions were defined as:

$$V = L_{00} + L_{10}w + L_{01}t + L_{20}w^2 + L_{11}wt + L_{02}t^2 \quad (3)$$

where w , t represents wfs , wt , respectively. If the response V represents h , $L_{00}=0.479$, $L_{10}=0.065$, $L_{01}=0.45$, $L_{20}=-0.001$, $L_{11}=-0.01$, $L_{02}=-0.0325$; else if V represents d , $L_{00}=3.94$, $L_{10}=-0.282$, $L_{01}=0.832$, $L_{20}=0.04$, $L_{11}=0.153$, $L_{02}=-0.1126$.

Table II lists the fitting results d_p and Δh_p , with the corresponding error, between the fitting value and the measured geometry, calculated by:

$$E_w = \frac{|e_p - e_m|}{e_m} \times 100\% \quad (4)$$

where e represents d and h respectively.

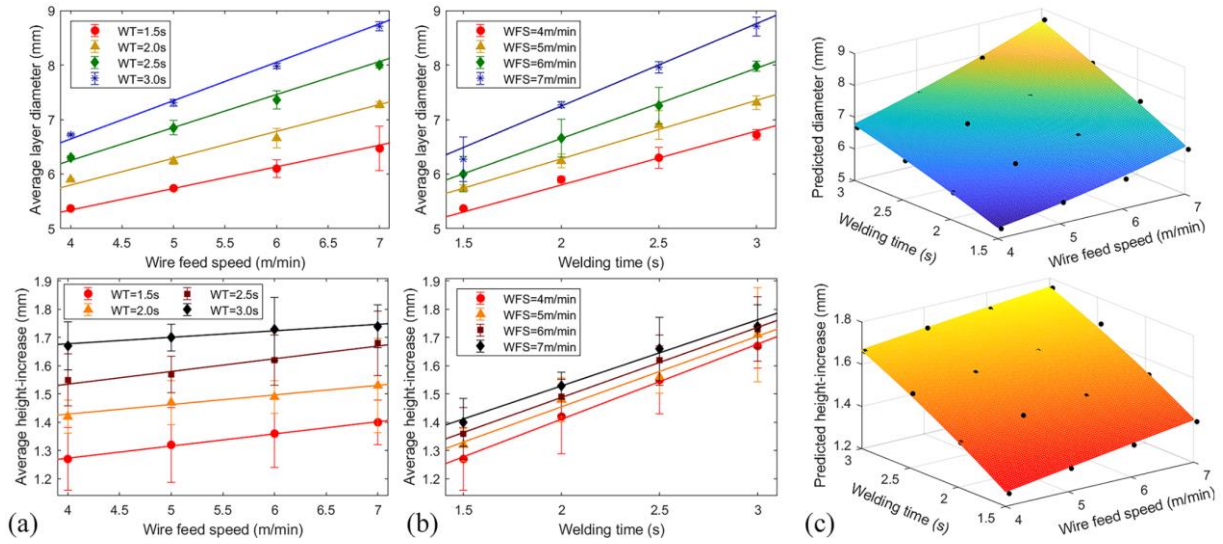


Fig. 4 The effect of (a) WFS, (b) WT on the layer geometry, and (c) fitting result.

Table II Process parameters and layer geometry formation

No	Process parameter		Measured results		Fitting results		Error (%)	
	wt (s)	wfs (m/min)	d_m (mm)	Δh_m (mm)	d_p (mm)	Δh_p (mm)	E_d (mm)	E_h (mm)
1	1.5	4.0	5.37	1.27	5.363	1.272	0.13	0.14
2	2.0	4.0	5.90	1.42	5.889	1.420	0.19	0.01
3	2.5	4.0	6.30	1.55	6.358	1.552	0.92	0.14
4	3.0	4.0	6.72	1.67	6.771	1.668	0.76	0.12
5	1.5	5.0	5.74	1.32	5.668	1.317	1.26	0.26
6	2.0	5.0	6.34	1.48	6.270	1.460	1.10	1.35
7	2.5	5.0	7.02	1.56	6.816	1.587	2.90	1.74
8	3.0	5.0	7.31	1.71	7.306	1.698	0.05	0.69
9	1.5	6.0	5.94	1.36	6.052	1.360	1.88	0.01
10	2.0	6.0	6.66	1.49	6.731	1.499	1.06	0.59
11	2.5	6.0	7.26	1.62	7.354	1.621	1.29	0.06
12	3.0	6.0	7.88	1.73	7.920	1.727	0.51	0.17
13	1.5	7.0	6.23	1.40	6.515	1.403	4.57	0.18

14	2.0	7.0	7.37	1.53	7.270	1.536	1.35	0.40
15	2.5	7.0	7.69	1.68	7.970	1.654	0.12	1.58
16	3.0	7.0	8.71	1.74	8.613	1.755	1.11	0.84

The normalized analysis is provided to compare the variation between measured values and predicted data, as shown in Fig. 5. All data is firstly normalized to X_i , which is determined by:

$$X_i = \frac{2}{R_{max} - R_{min}} (R_i - R_{min}) - 1 \quad (5)$$

where R_{max} , R_{min} is the raw max, min data of the average actual measured data, respectively. The solid orange line ($y = x$) shown in Fig. 5 indicates that the measured values closely match their predicted counterpart. In this figure, all the normalized points are close to the line, indicating the proposed strut-based bead modelling is able to accurately predict the layer geometry of a well-formed strut within a given range.

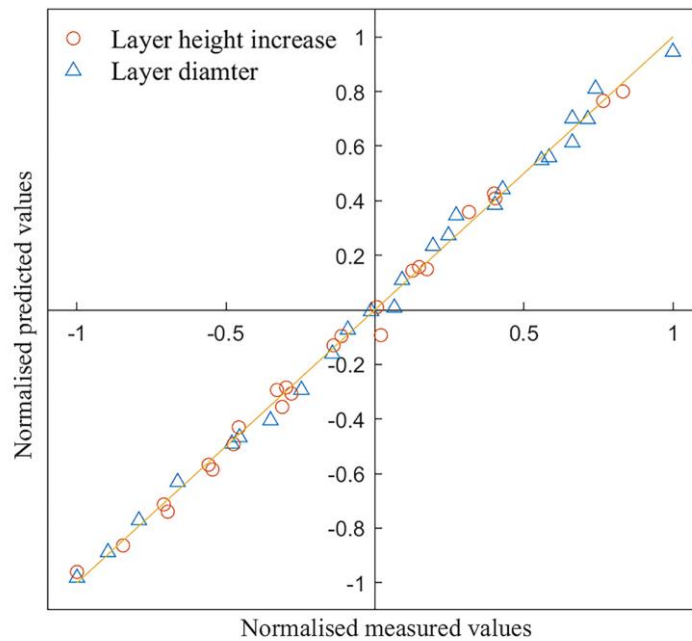


Fig. 5 Comparison between predicted and measured value (normalized).

Except for bead modelling established for vertical-down deposition, it must also ascertain the layer geometry formation of the strut with the inclined angle. In WAAM, the welding pool that provides the surface tension can counter gravitational forces during the welding process. For each deposit, the Eotvos number E_o reported in [8] is used to represent the gravity force effect relative to surface tension, expressing as:

$$Eo = \frac{\Delta\rho g L^2}{4\gamma} \quad (6)$$

where γ and $\Delta\rho$ are obtained from **Table I**. L is defined as the characteristic length. Here it is considered as the layer diameter d . As a general rule, when $Eo < 1$ (that is, $d < 9\text{mm}$), the molten pool is able to maintain at the required position predominantly supported by the surface tension [8]. Therefore, it is concluded that the depositing process can be performed at any given arbitrary angle under the process parameter combinations studied in the proposed bead modelling. For struts with different angles, their layer geometries are only related to the welding parameters wfs and wt , but not the incline angle. Fig. 6 demonstrates these findings, where a number of struts were deposited with a strut angle varying from 30 to 90 degrees.

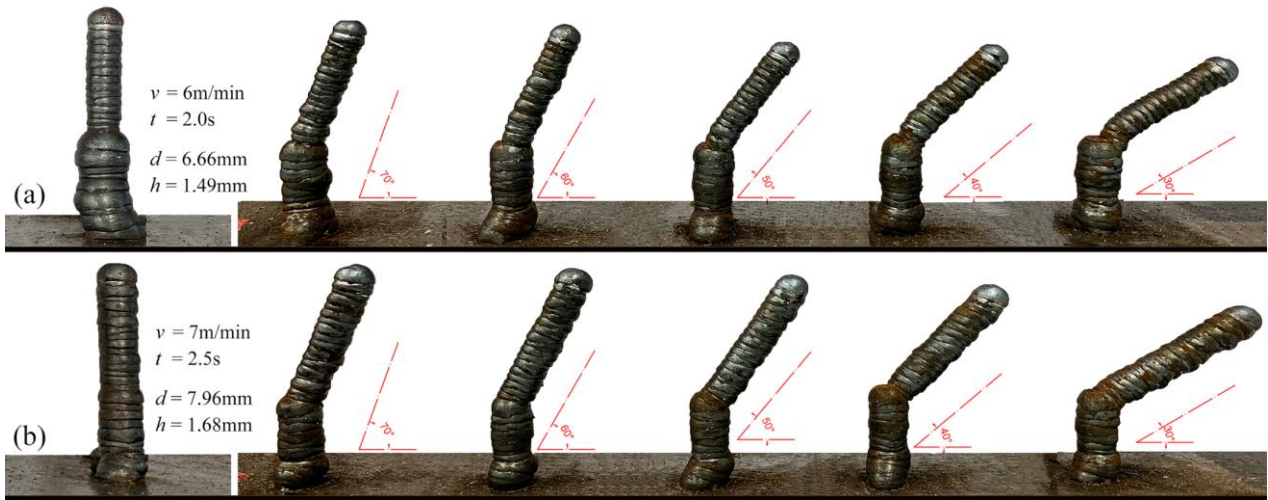


Fig. 6 Some appearance of struts with incline angles (30° to 90°).

4.2 Height control system

As mentioned previously, there will be some deviation between the actual height of a deposited bead and the predicted height. As the manufacturing process continues, this may also cause cumulative errors. This can significantly skew the overall geometry of the deposited part. To overcome this challenge, the paper proposes an alternative method using lag control to adjust the welding point when the actual height-increment of a layer does not match the theoretical one.

To do this, $ctwd$ (c) is used as the study object to find the effect of its change on welding current and voltage. A number of tests were conducted, where the test range of c is from 4mm to 24mm, during which $wfs = 4\text{m/min}$, $wt = 2\text{s}$. The acquisition value of the welding current and welding voltage is the

average value, and the sampling frequency is 2000hz. The results are presented in Fig. 7. The current remains relatively constant at 60A but becomes more and more unstable as the c increases. And the voltage has a positive linear correlation with the change of it, which means if the voltage is recorded during each welding process, the actual Δh_a can be calculated by the difference between the c used in the bead modelling and the actual c_a shown by the voltage. It is worth mentioning that this method records the relationship between c and voltage, so it always assumes that the height-increment of the current deposit layer is Δh .

When the deposition process of a layer is completed, the welding torch will shift the distance Δh to the next layer, regardless of the real height-increment of the current layer. Then, during the processing phase for the next layer, if the recorded voltage V_a is different from the corresponding value for c , the position must be adjusted accordingly.

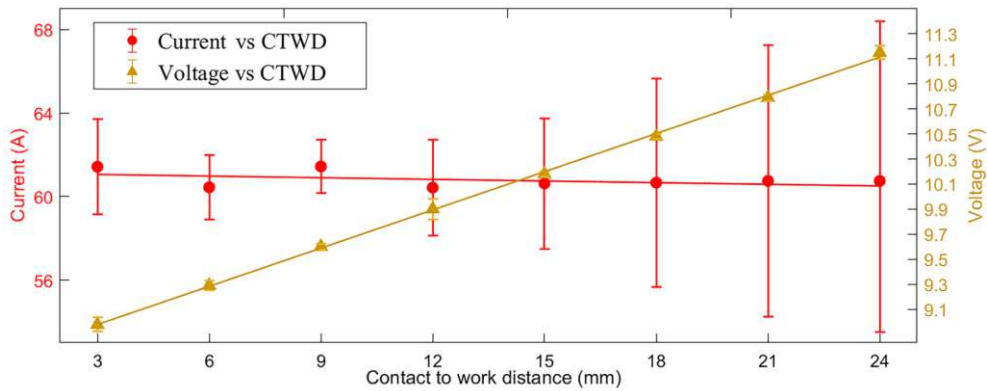


Fig. 7 Changes of welding current and voltage under different CTWD, here $V_i=0.1017c + 8.673$.

4.3 Adaptive Slicing Methodology

Combined with the height control system, an adaptive slicing algorithm is proposed to find the deposition points for each strut part. The first step is to extract the centroidal axes (or skeleton) of the complete wire structure. This will reduce the volumetric nature of the part to a more simplistic representation of points and lines. Next, we have the task of determining a) the total number of individual struts s_i in the part, and b) the total number of layers $L_{i,n}$ contained in each of these struts.

Each strut in the part is defined by two feature points: namely, the start point n_{i_1} and the end point n_{i_2} . So, the strut is expressed as $s_i = [n_{i_1}, n_{i_2}]$. For any particular strut, no matter how complex its direction of growth, if it shares its start point n_{i_1} with the end point of a different strut n_{j_2} And its

end point n_{i_2} is shared with a start point of a different strut n_{j_1} , then the strut between these two characteristic points can be defined as an independent strut, as an example shown in Fig. 8 (b).

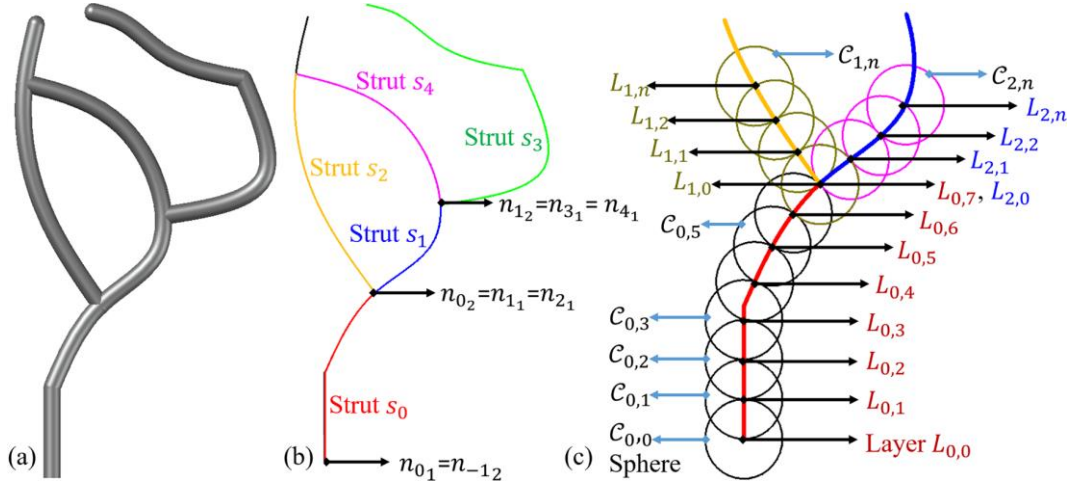


Fig. 8 Schematic diagrams of slicing methods. (a) Wire structure model, (b) Acquisition of independent struts, (c) Proposed strut slicing method.

After the classification of the individual struts is complete, the next step is to determine the number of layers $L_{i,n}$ belonging to each strut s_i . A simplistic approach, which splits the central axis of each strut into linear segments of length Δh , may seem logical, but ultimately will not suffice in cases where the strut's direction of growth changes, this approach will not accurately capture the actual height increment added during the deposition process. To overcome this, a different approach is proposed, as outlined in Fig. 8 (c). In this method, a sphere $C_{i,0}$ with a radius of Δh , is used to slice each strut. The sphere is centered at the starting point of the first strut $L_{0,0}$ and the intersection of the sphere and s_0 is then used to define the deposition point of the next layer $L_{i,1}$. This process continues until all struts are processed. The deposition points for each layer $L_{i,n}$ are calculated by the intersection point of the sphere surface generated through the previous layer $L_{i,n-1}$. The coordinates for the point in the strut s_i , can be defined as:

$$L_{i,m+1_{x,y,z}} = C_{i,n} \cap S_{tot} - L_{i,m-1_{x,y,z}} \quad (7)$$

where $C_{i,n}$ is a set containing all the data $\{4\pi\vec{h}i^2\}$ on the sphere $C_{i,n}$, $\vec{h}i$ is used as a vector with a modulus of Δh pointing in all directions, and S_{tot} is a set containing all coordinates of s_i . However, the representation of $\vec{h}i$ as a vector will entail a heavy computation load. To reduce computational magnitude, all data in the set $C_{i,n}$, are then represented by spherical coordinates:

$$\{4\pi\vec{h}i^2\} = \{M(x, y, z) | x = r\sin\varphi\cos\theta, y = r\sin\varphi\sin\theta, z = r\cos\varphi\} \quad (8)$$

where $0 \leq r \leq \infty$, $0 \leq \varphi \leq 2\pi$, $0 \leq \theta \leq \pi$. Here $r = |\vec{h}i|$, φ is a half-plane formed by the z-axis and the plane ZOY, and θ represents the angle between r and the positive direction of the z-axis.

The algorithm divides a strut s_i with total length S_{tot} into polylines of n layers with equal length Δh . It is worth noting that sometimes the strut may not be divided exactly into n layers with the selected Δh . In these situations, the number of layers n in a strut can then be rounded up.

The overall method is presented as a flow chart shown in Fig. 9. It is worth noting that the robot pose adjustment refers to the tool center point position (welding torch-tip). Welding position and rotation are derived from the parts coordinates and the building direction of each layer in the strut.

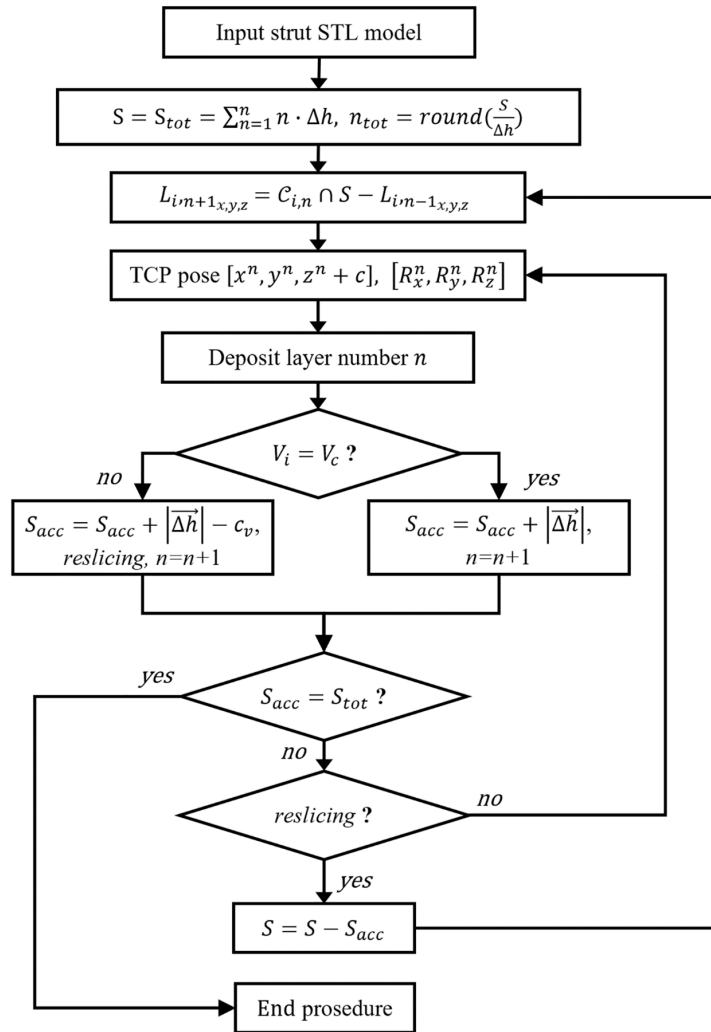


Fig. 9 Processes of the slicing and height control methods for the strut.

Combined with the height control system, the effectiveness of this adaptive slicing methodology is elaborated in Fig. 10, in which two arc-shaped struts are manufacturing with or without the present adaptive slicing method. Fig. 10 (a) shows the strut fabricated successfully via the proposed adaptive method. While with a constant slicing height, as shown in Fig. 10 (b). Fig. 10 (c) also shows a scenario, which is characterized by the accumulation of positional errors in the static approach as the depositing process continues, thereby destroying the final geometric formation of the strut.

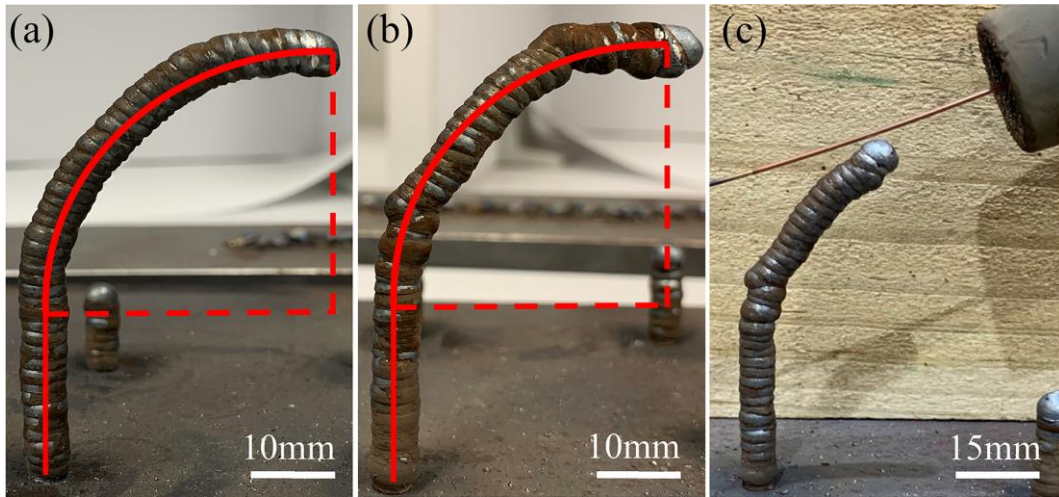


Fig. 10 Arc-shaped strut deposition process (a) with adaptive CTWD changes, (b) in static deposition approach; (c) Cumulative errors in (b) discontinues the deposition.

4.4 Handling Branch Intersection

The intersections of a wire structure occur where two or more struts' end points merge together, which is defined as a convergence node; when the same end points of struts correspond to the start points of two or more new struts, then it is called a divergence node, as shown in Fig. 11. As the deposition process for a given strut nears these nodes, some strategies need to be employed to avoid poor weld bead geometry or potential collision between the torch nozzle and the component.

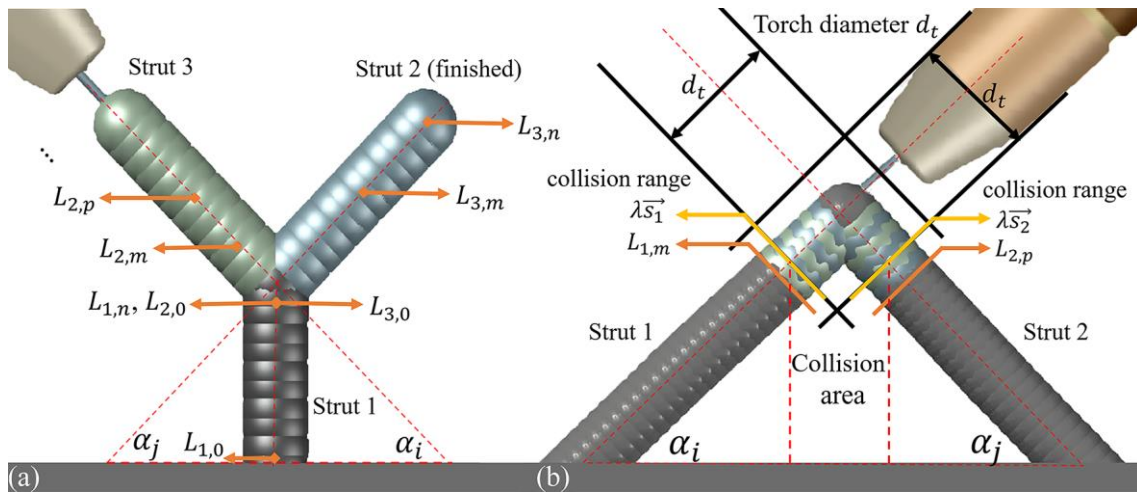


Fig. 11 The example of (a) the divergence node and (b) the convergence node.

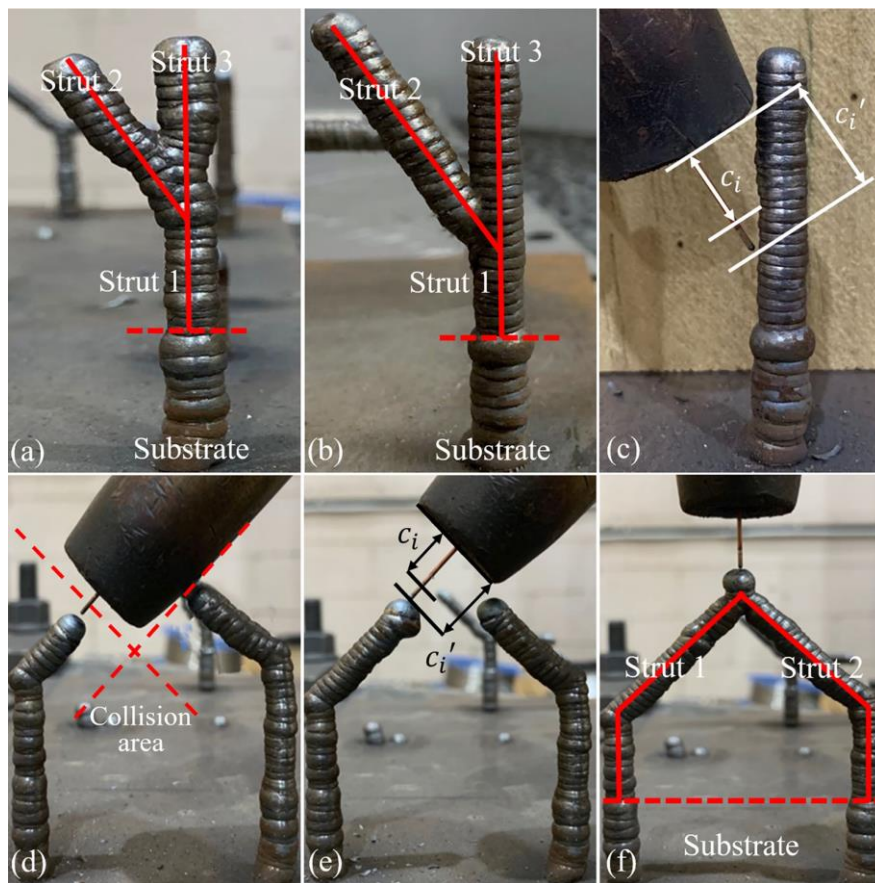


Fig. 12 Examples of fabricating branch intersections. For divergence samples: (a) deposit layer-by-layer in the traditional z-direction; (b) deposit strut-by-strut in order; (c) The adaptive changes of CTWD used to avoid collisions. For convergence nodes: (d) determining the collision area (collision layer); (e) The adaptive changes of CTWD used to avoid collisions; (f) the final geometry of this sample.

For struts emanating from a divergence node, two build options are available. First, the struts could be deposited by alternating the deposition process evenly between them, so in-effect, they are built up simultaneously. Alternatively, each strut can be deposited individually in one shot according to

their strut number i , as shown in Fig. 11 (a). The first method usually produces poor strut geometry, as shown in Fig. 12 (a). This is mainly due to the slippage of the molten pool during the welding process. The molten pool is prone to be adsorbed towards the adjacent strut whose material has already been deposited so that the deposition process does not proceed in the expected position, resulting in a deformed structure. To avoid this phenomenon, struts at this point need to be continuously deposited and manufactured one-by-one according to their corresponding processing sequence, as shown in Fig. 12 (b). CTWD is also needed to be dynamically adjusted so as to prevent the torch from collides with deposited struts if they have a small included angle, as shown in Fig. 12 (c).

4.5 Tool Path Planning Strategy

The tool path planning strategy is then presented for processing a complete wire structure. The wire structure, which is expressed as $\mathcal{W} = \{\mathcal{S}, \mathcal{N}\}$, can be represented as intersection points set $\mathcal{N} = \{n_i \mid i = 1, 2, 3, \dots, |\mathcal{N}|\}$, and individual struts set $\mathcal{S} = \{s_i \mid i = 1, 2, 3, \dots, |\mathcal{S}|\}$. The first step in the path planning process is to identify struts that share the same convergence or divergence nodes. Any independent strut except for struts connected to the substrate must have a convergence node and a divergence node. Thus, for all struts $s_1, s_2, s_3, \dots, s_i = [n_{i_1}, n_{i_2}]$, these which have the same start point are then put in the same set $\mathcal{S}_{\mathcal{P}_m}^{div}$, defined as:

$$\mathcal{S}_{\mathcal{P}_m}^{div} = \{s_i \mid n_{i_1} = n_{j_1}, i \in (1, |\mathcal{N}|), j \in (1, |\mathcal{N}|)\} \quad (9)$$

where $\mathcal{P}_m = \{i \mid n_{i_1} = n_{j_1}, i \in (1, |\mathcal{N}|), j \in (1, |\mathcal{N}|)\}$

Therefore, all struts in \mathcal{S}^{div} that have the same start point is labeled as \mathcal{P}_m . Correspondingly, all struts which share the same particular end point are defined as:

$$\mathcal{S}_{\mathcal{P}_m}^{cov} = \{s_i \mid n_{i_2} = n_{j_2}, i \in (1, |\mathcal{N}|), j \in (1, |\mathcal{N}|)\} \quad (10)$$

where $\mathcal{P}_m = \{i \mid n_{i_2} = n_{j_2}, i \in (1, |\mathcal{N}|), j \in (1, |\mathcal{N}|)\}$.

The build sequence of struts should be arranged in terms of their end point height (from low-to-high in the z-axis) to avoid a scenario where higher struts are processed blocking access for the welding

torch to deposit underneath struts. After that, a valid deposition sequence is ready to be generated.

As logic dictates, any given strut is supposed to have two or more struts underneath it to provide support (i.e., all struts will emanate from a node of two or more struts). This means that the end point of any strut will also be the start point in another strut. With this in mind, struts that successfully deposited are put into the set $\mathcal{S}_k^p = \{s_*^p, \dots, s_k^p\}$. Struts that have not yet deposited or will be deposited soon are defined as,

$$\mathcal{S}_k^u = \mathcal{S} \setminus \mathcal{S}_k^p \quad (11)$$

When planning a deposition sequence, convergence nodes are used as the basis for the analysis. First, for a given convergence node, a search for all the struts which converge upon it is performed. Then, all struts in the set will be traversed to find whose end points are consistent with the start points of the struts at this point, expressed as,

$$\bigcap_{s_i \in \mathcal{S}_{p_m}^{con}} (\mathcal{N}_{i_1}, \mathcal{S}_k^p) \neq \emptyset \quad (12)$$

where
$$\mathcal{N}_{i_1} = \{n_{j_2} \mid n_{s_{i_1}} = n_{s_{j_2}}, s_i \in \mathcal{S}_{p_m}^{cov}, s_j \in \mathcal{S}\}$$

The role of \mathcal{N}_{i_1} is that for any strut in the set $\mathcal{S}_{p_m}^{con}$, it will iterate all other struts which share the same end point n_{j_2} as its start point n_{i_1} . This element is then compared one-by-one with each element in \mathcal{S}_k^p . Only when \mathcal{S}_k^p contains all the same elements as in \mathcal{N}_{i_1} , can a valid processing sequence be established. The example shown below in Fig. 13 illustrates this process.

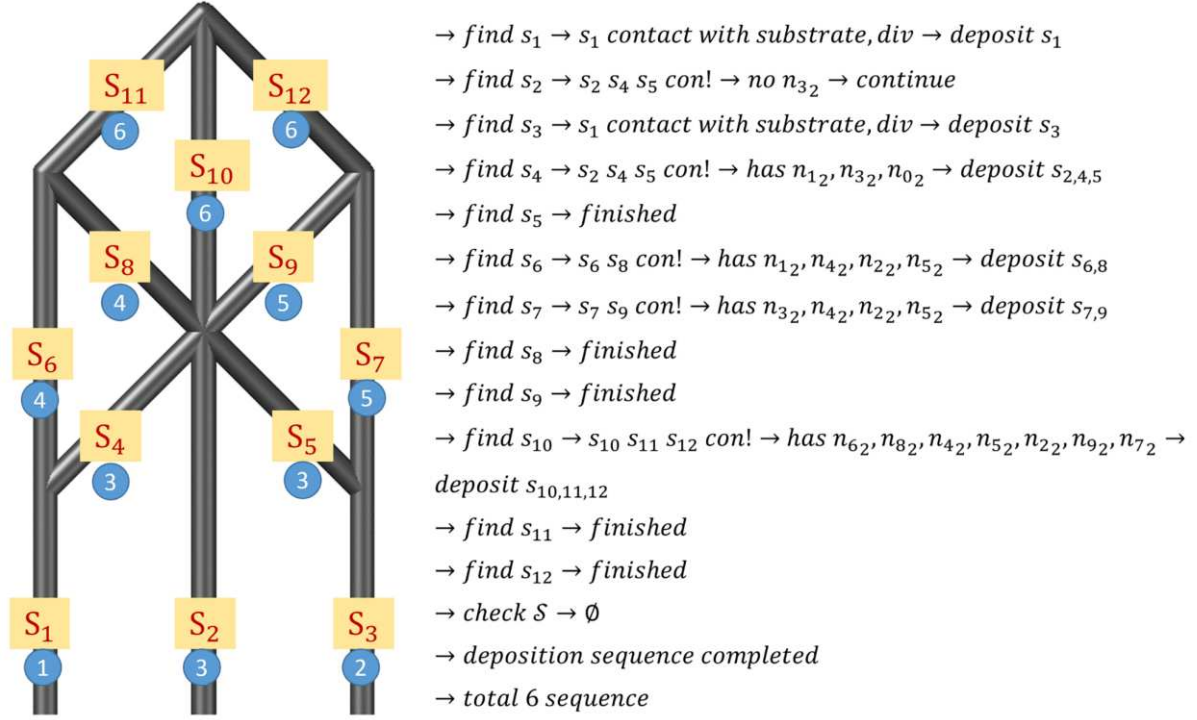


Fig. 13 An example of generating a deposition sequence for a wire structure.

The length of the wire stick-out of the welding torch can be adjusted within a reasonable range, making its path planning more flexible, as Yuan et al. [19] stated. Therefore, to achieve a proper and collision-free deposition sequence, the *ctwd* may need to be adjusted during the process. As mentioned previously, the struts in the set $\mathcal{S}_{P_m}^{cov}$ create a potential collision (between the torch and nearby struts) as the build nears a convergence node. If a strut s_i is treated as a vector, it has a higher probability of collision in the range $\lambda \vec{s}_i$, as shown in Fig. 11. The max collision area λ_{max} can be defined as:

$$\lambda_{max} = 1 - \max \left(\bigcup_{i=1, j=1}^n \frac{d_t |\vec{s}_i|}{\sqrt{|\vec{s}_i|^2 |\vec{s}_j|^2 - (\vec{s}_i \cdot \vec{s}_j)^2}} \right) \quad (13)$$

Struts must be compared one-by-one at this convergence point to determine the largest collision area. As shown in Fig. 12 (d) and (e), when the torch reaches the range of $(1 - \lambda_{max}) \vec{s}_i$, the *ctwd* should be increased to ascertain the welding torch is outside the collision area. Similarly, when processing the strut near the divergence point, a collision check must be performed.

5. Case studies

To further verify the performance of the proposed strategy, two parts featuring complex wire structures were fabricated. In these two case studies, the same filler material, shielding gas, substrate material, automatic welding system and all proposed fabrication strategy outlined in the previous section were used. The process parameters were maintained at $wfs=4\text{m/min}$, $wt=2\text{s}$ for all deposition processes.

5.1 The cube-shaped part fabrication process

Fig. 14 shows the first fabricated part, a cube-shaped item defined by 12 struts, as shown in Fig. 14 (a). The length of all struts is about 30mm, and the height of the main structure is about 52mm. This structure has approximately 260 deposition layers and six intersection points, of which both the number of divergence nodes and convergence nodes is 3. It has five processing sequences, where struts 1, 2, and 3 have no convergence feature points, so they are regarded as one processing procedure. The final cube-shaped part is presented in Fig. 14 (c). The cool-down time between each layer of the welding period was set to 30 seconds, and the total processing time of it was about 5 hours. Fig. 14 (d) illustrates some fabrication details of the layers near convergence nodes. Through the (13), the λ_{max} for all struts in the same convergence node is 0.667, which means that when the height of a strut in its build direction reaches about 20mm, it is necessary to deposit all the struts in the same processing sequence layer-by-layer with their own layer number n .

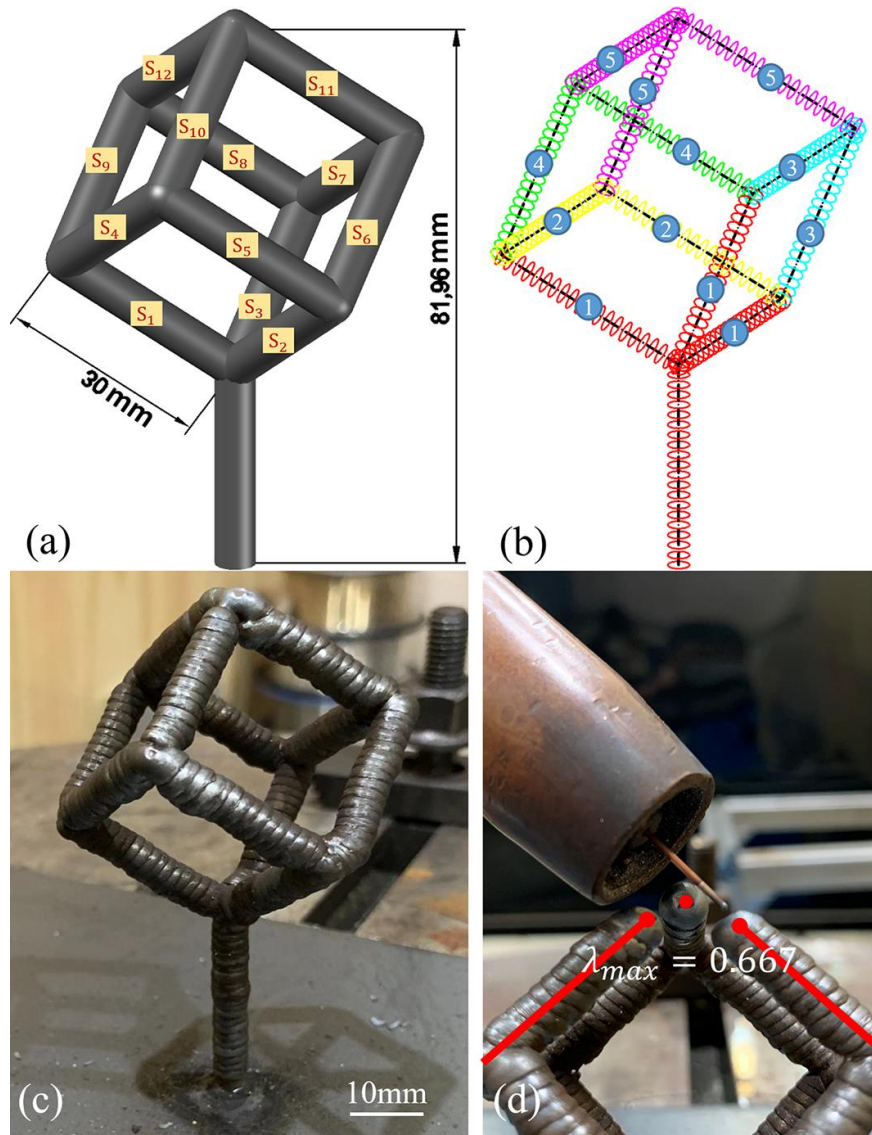


Fig. 14 Cube-shaped wire structure. (a) The STL model, (b) the slicing model, (c) the final part, and (d) a fabrication detail.

5.2 honeycomb-part fabrication process

Fig. 15 shows the second fabricated part: A honeycomb-like part consisting of wire structures. Its main structure contains a total of 24 struts. It has approximately 640 deposition layers with a total of 14 intersection points and a total of 12 processing sequences. The length of all struts is 30mm. The height is about 150 mm, and the maximum width of it in the x-axis direction is about 156mm. The final honeycomb-shaped part is presented in Fig. 15 (b). Its cool-down time between each layer of the welding period was also set to 30 seconds, and the total processing time of it was about 10 hours. the collision range λ_{max} for all the struts is 0.6151. Therefore, when the height of the strut reaches about 18.45mm, it is necessary to deposit them layer-by-layer.

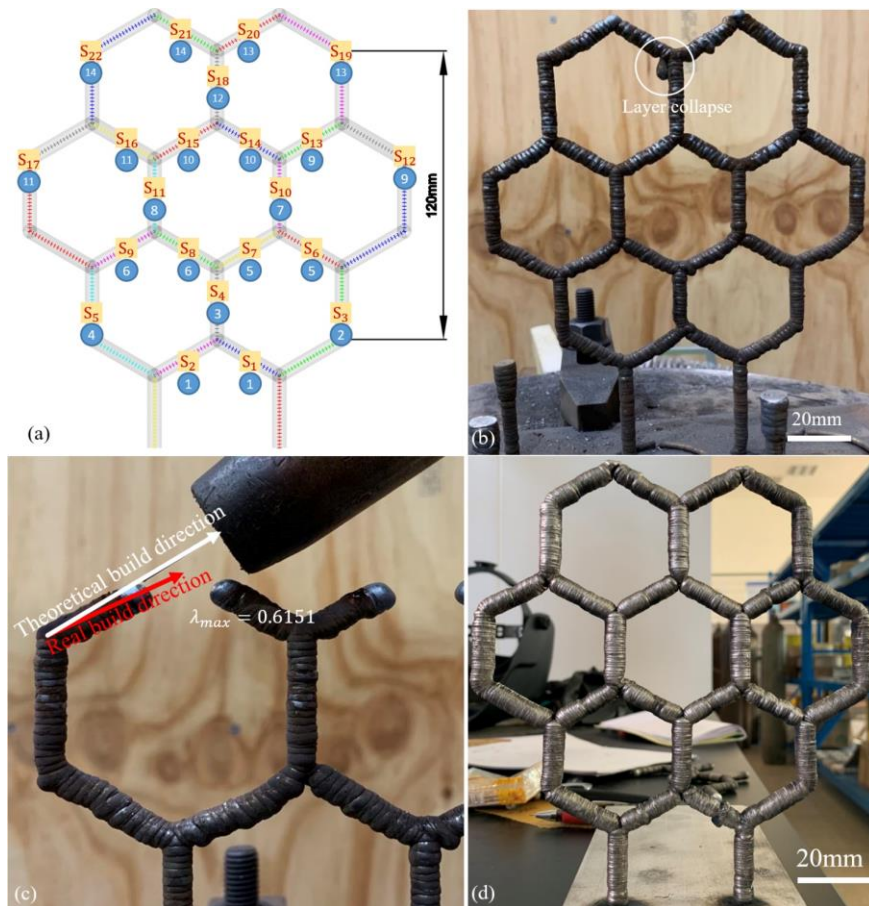


Fig. 15 Honeycomb-shaped wire structure. (a) The slicing model, (b) the part (mild steel), (c) the problem encountered in processing, and (d) the part (aluminum ER4043) with $v=5\text{m/min}$, $t=1\text{s}$, $d=9\text{mm}$, and $h=1\text{mm}$.

Fig. 15 (c) highlights a problem in the fabrication process. Due to the effect of heat accumulation, the cooling time of 30 seconds is not enough to cool it down to a suitable temperature range. The additional heat build-up affects the solidification process, and as a result, the build direction of the strut was observed to droop somewhat. This was not observed in the cube structure, as the inclined angles of the struts were less. In more severe cases, the deposit was observed to spill off the build layer before solidification. To address this, further experiments will make use of a temperature camera to monitor interpass temperatures of the welding process to adjust the cooling time dynamically. The influence of temperature on the strut can also be investigated in-depth via a detailed bead modelling study.

Moreover, the strategy proposed in the paper is robust and adaptive for almost all metal materials, as long as it can be given stable welding parameters. As an extra example shown in Fig. 15 (d), this is the same honeycomb structure processed with aluminum ER4043 (bead modelling not explained here). In conclusion, the quality result of the obtained resultant geometry for these two steel parts and

one aluminum part with the wire structure, particularly at intersection nodes, is good-looking and precise in position, highlighting the reliability and practicality of the fabrication strategy proposed in this paper.

6. Conclusion

In this work, a WAAM fabrication strategy for manufacturing components featuring wire structures via the point-by-point manner was presented. Firstly, a strut-based bead modelling process was well established to accurately ascertain and predict the optimal welding process parameters for the selected bead geometry of the given strut. Subsequently, the adaptive slicing algorithm and height control system of the strut was also presented to generate an adaptive slicing model. Then these items are used in combination for the torch path planning of the overall deposition process. Finally, their effectiveness was elaborated through the fabrication process of two separate parts featuring wire structure designs.

Further research aims to enhance the practicality of the proposed strategy and further develop the robotic system to deposit these wire structures reliably. The topology optimization process will be regarded as a research and development focus to split the entire workpiece into multiple independent regions, thereby reducing the time spent on processing workpieces with high space complexity. The work will also expand reliable and robust algorithms to reduce the weight of physical workpieces or convert them into stable skeleton-structures and manufacturing arbitrary workpieces that combine wire structures and thin-walled structures and solid structures, etc.

Acknowledgment

This work was supported in part by the National Natural Science Foundation of China under Grant 51805085, in part by the China Scholarship Council under Grant 201908200010.

Declarations

Funding: This work was supported in part by the National Natural Science Foundation of China under Grant 51805085, in part by the China Scholarship Council under Grant 201908200010.

Conflicts of interest: Not applicable.

Availability of data and material: Not applicable.

Code availability: Not applicable.

Authors' contributions: Not applicable.

Ethics approval: Not applicable.

Consent to participate: Not applicable.

Consent for publication: Not applicable.

References

1. Gibson I, Rosen D, Stucker B, et al (2015) Directed Energy Deposition Processes. *Addit Manuf Technol* 245–268. https://doi.org/10.1007/978-1-4939-2113-3_10
2. Ding D, Pan Z, Cuiuri D, Li H (2015) Wire-feed additive manufacturing of metal components: technologies, developments and future interests. *Int J Adv Manuf Technol* 81:465–481. <https://doi.org/10.1007/s00170-015-7077-3>
3. Williams SW, Martina F, Addison AC, et al (2016) Wire + Arc additive manufacturing. *Mater Sci Technol (United Kingdom)* 32:641–647. <https://doi.org/10.1179/1743284715Y.0000000073>
4. Shen C, Pan Z, Ding D, et al (2018) The influence of post-production heat treatment on the multi-directional properties of nickel-aluminum bronze alloy fabricated using wire-arc additive manufacturing process. *Addit Manuf* 23:411–421. <https://doi.org/10.1016/j.addma.2018.08.008>
5. Yilmaz O, Uгла AA (2016) Shaped metal deposition technique in additive manufacturing: A review. *Proc Inst Mech Eng Part B J Eng Manuf* 230:1781–1798. <https://doi.org/10.1177/0954405416640181>
6. Guo N, Leu MC (2013) Additive manufacturing: Technology, applications and research needs. *Front Mech Eng* 8:215–243. <https://doi.org/10.1007/s11465-013-0248-8>
7. Ngo TD, Kashani A, Imbalzano G, et al (2018) Additive manufacturing (3D printing): A review of materials, methods, applications and challenges. *Compos Part B Eng* 143:172–196. <https://doi.org/10.1016/j.compositesb.2018.02.012>
8. Radel S, Diourte A, Soulié F, et al (2019) Skeleton arc additive manufacturing with closed loop control. *Addit Manuf* 26:106–116. <https://doi.org/10.1016/j.addma.2019.01.003>
9. Huang Y, Zhang J, Hu X, et al (2016) FrameFab : Robotic Fabrication of Frame Shapes. *35:1–11*
10. Mueller S, Im S, Gurevich S, et al (2014) WirePrint: Fast 3D Printed Previews. *Proc UIST*

11. Li Y, Yu S, Chen Y, et al (2020) Wire and arc additive manufacturing of aluminum alloy lattice structure. *J Manuf Process* 50:510–519. <https://doi.org/10.1016/j.jmapro.2019.12.049>
12. MX3D (2018) MX3D projects. <https://mx3d.com/>
13. Wu B, Pan Z, Ding D, et al (2018) A review of the wire arc additive manufacturing of metals: properties, defects and quality improvement. *J Manuf Process* 35:127–139. <https://doi.org/10.1016/j.jmapro.2018.08.001>
14. Ding D, Shen C, Pan Z, et al (2016) Towards an automated robotic arc-welding-based additive manufacturing system from CAD to finished part. *CAD Comput Aided Des* 73:66–75. <https://doi.org/10.1016/j.cad.2015.12.003>
15. Yuan L, Ding D, Pan Z, et al (2020) Application of Multi-directional Robotic Wire Arc Additive Manufacturing Process for The Fabrication of Complex Metallic Parts. *IEEE Trans Ind Informatics* 16:1–1. <https://doi.org/10.1109/tii.2019.2935233>
16. Xu J, Gu X, Ding D, et al (2018) A review of slicing methods for directed energy deposition based additive manufacturing. *Rapid Prototyp. J.* 24:1012–1025
17. Wu R, Peng H, Guimbretière F, Marschner S (2016) Printing arbitrary meshes with a 5DOF wireframe printer. *ACM Trans Graph* 35:1–9. <https://doi.org/10.1145/2897824.2925966>
18. Luo Y, Li J, Xu J, et al (2018) The CMT short-circuiting metal transfer process and its use in thin aluminium sheets welding. *Mater Des* 30:1850–1852. <https://doi.org/10.1016/j.matdes.2008.07.015>
19. Yuan L, Pan Z, Ding D, et al (2020) Fabrication of metallic parts with overhanging structures using the robotic wire arc additive manufacturing. *J Manuf Process* 0–1. <https://doi.org/10.1016/j.jmapro.2020.03.018>

Figures

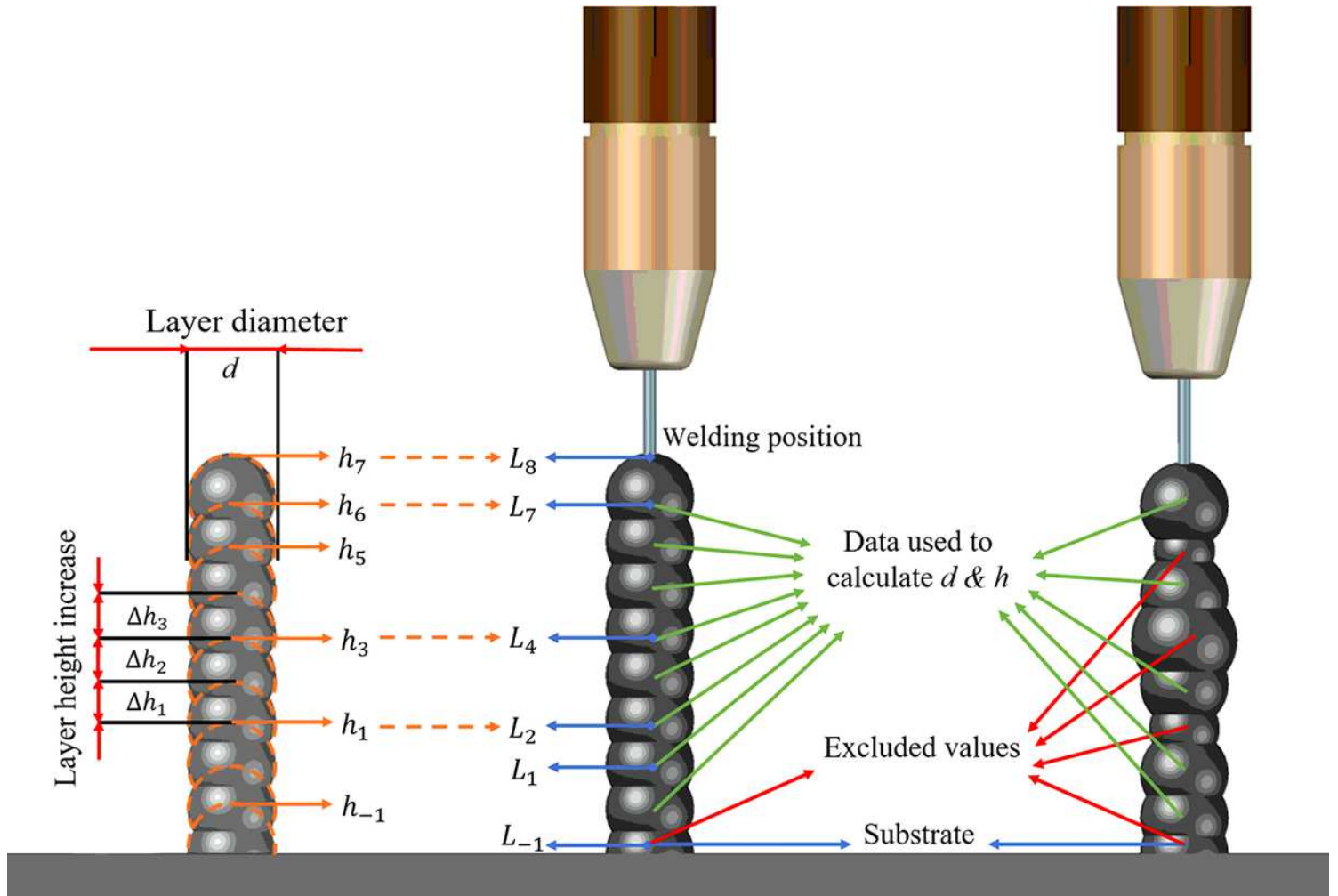


Figure 1

Definition of layer geometry, substrate, and layer data collected.

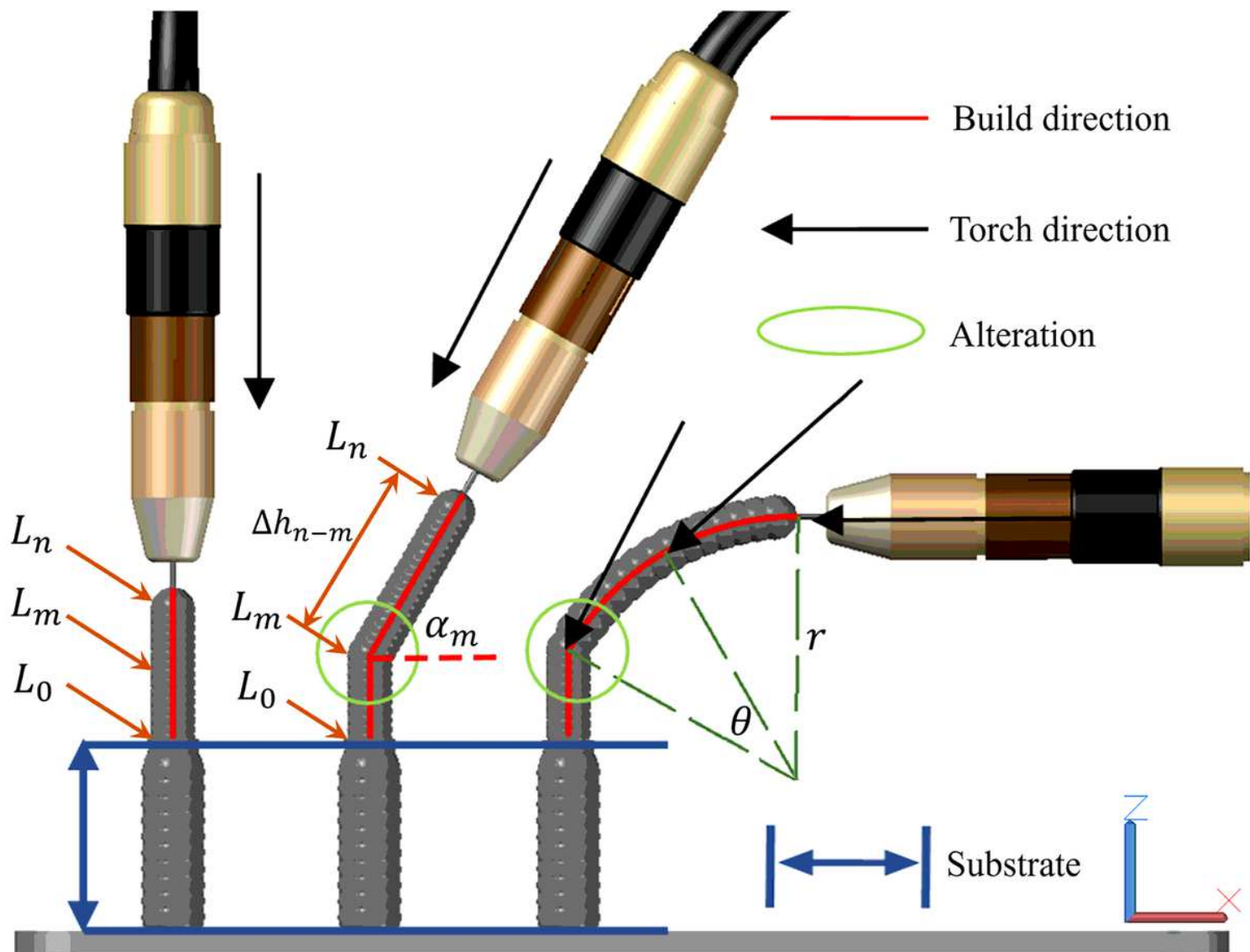


Figure 2

The schematic of the build direction, torch direction of the single strut.

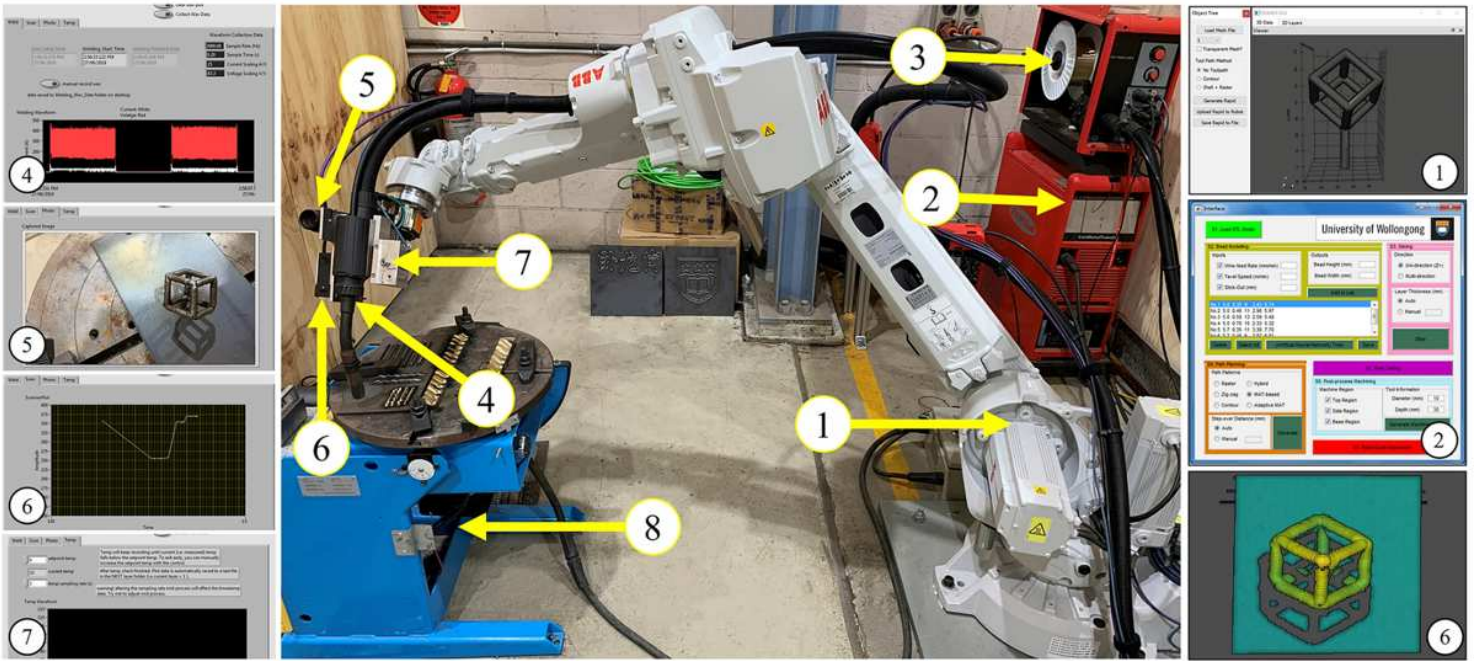


Figure 3

WAAM system. (1) IRB 2600; (2) TransPuls Synergic 5000 CMT welder; (3) VR 7000 CMT wire feeder; (4) CMT torch; (5) CCD camera; (6) 3D profile scanner; (7) Infrared temperature sensor; (8) 2-DOF workpiece positioner.

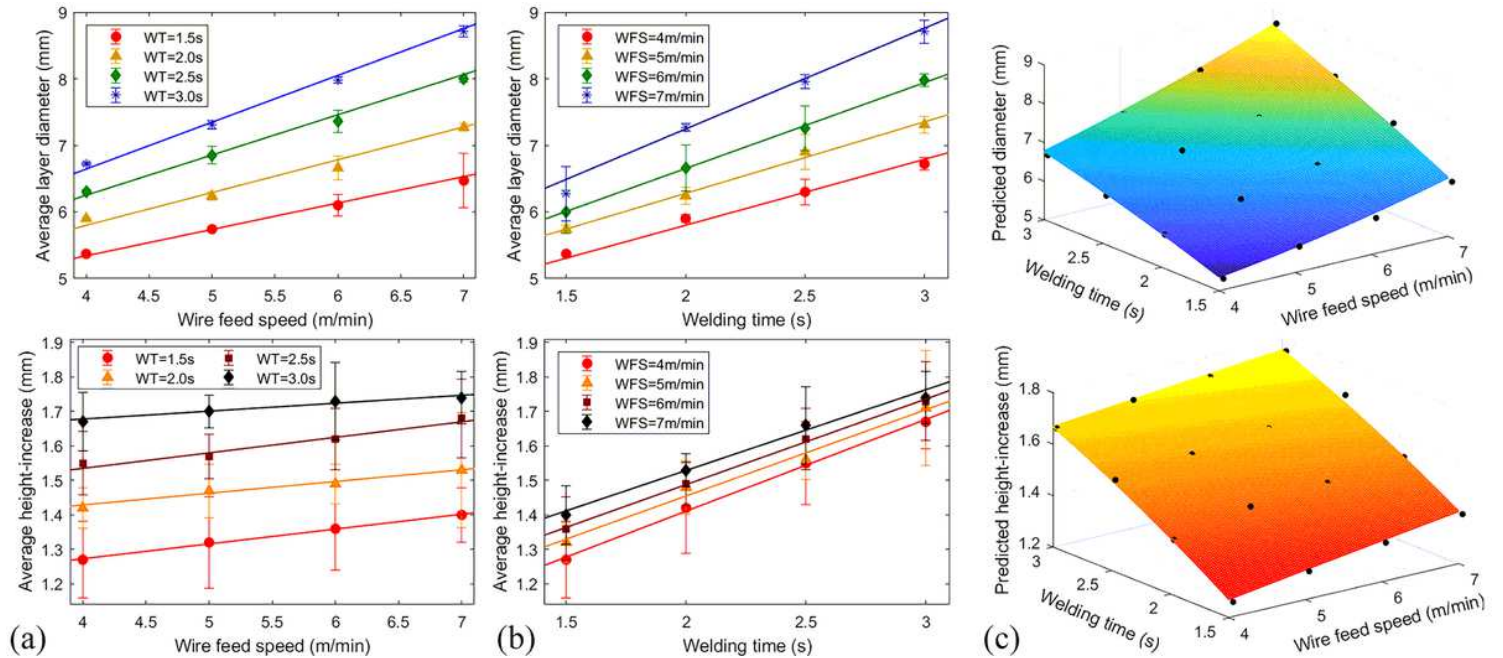


Figure 4

The effect of (a) WFS, (b) WT on the layer geometry, and (c) fitting result.

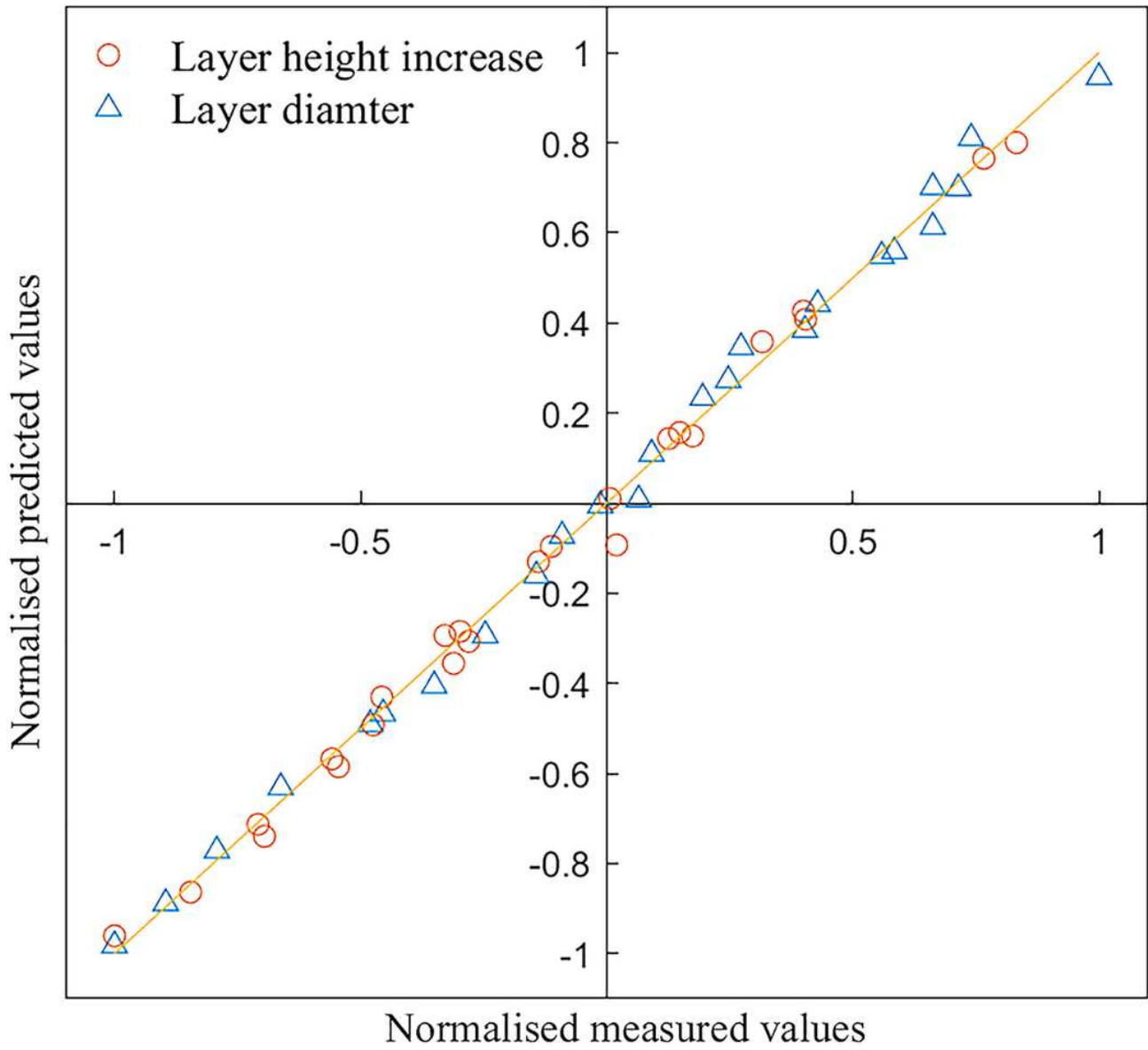


Figure 5

Comparison between predicted and measured value (normalized).

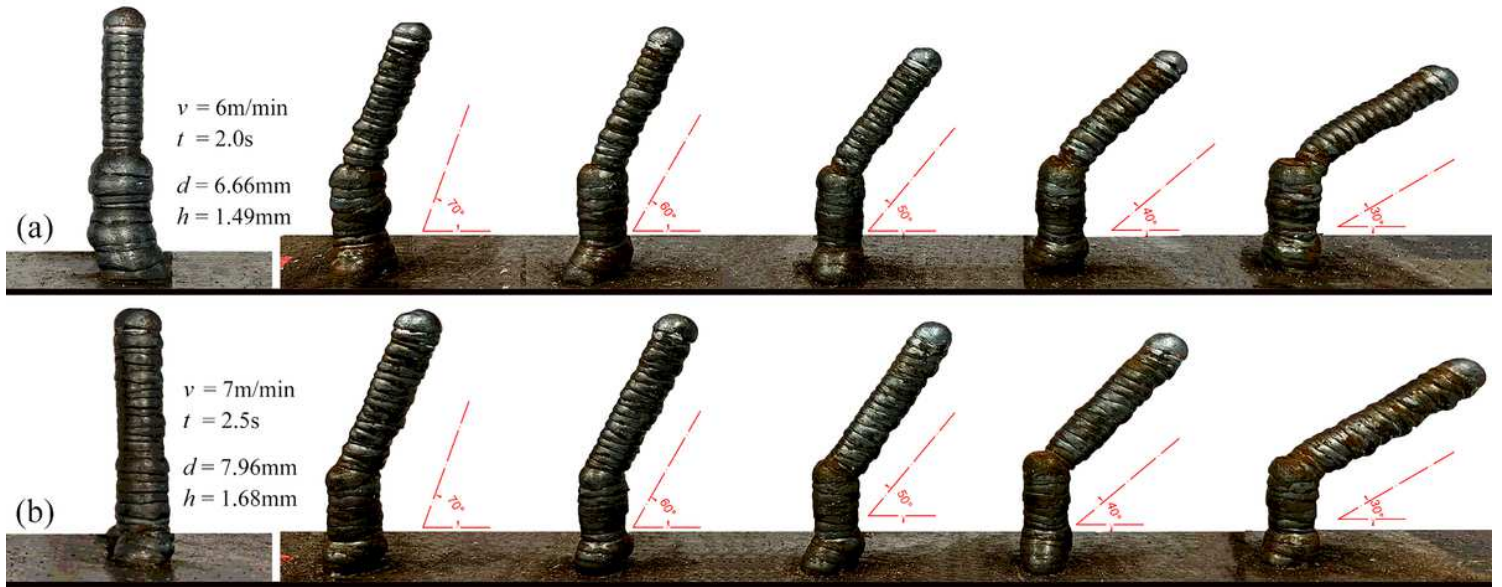


Figure 6

Some appearance of struts with incline angles (30° to 90°).

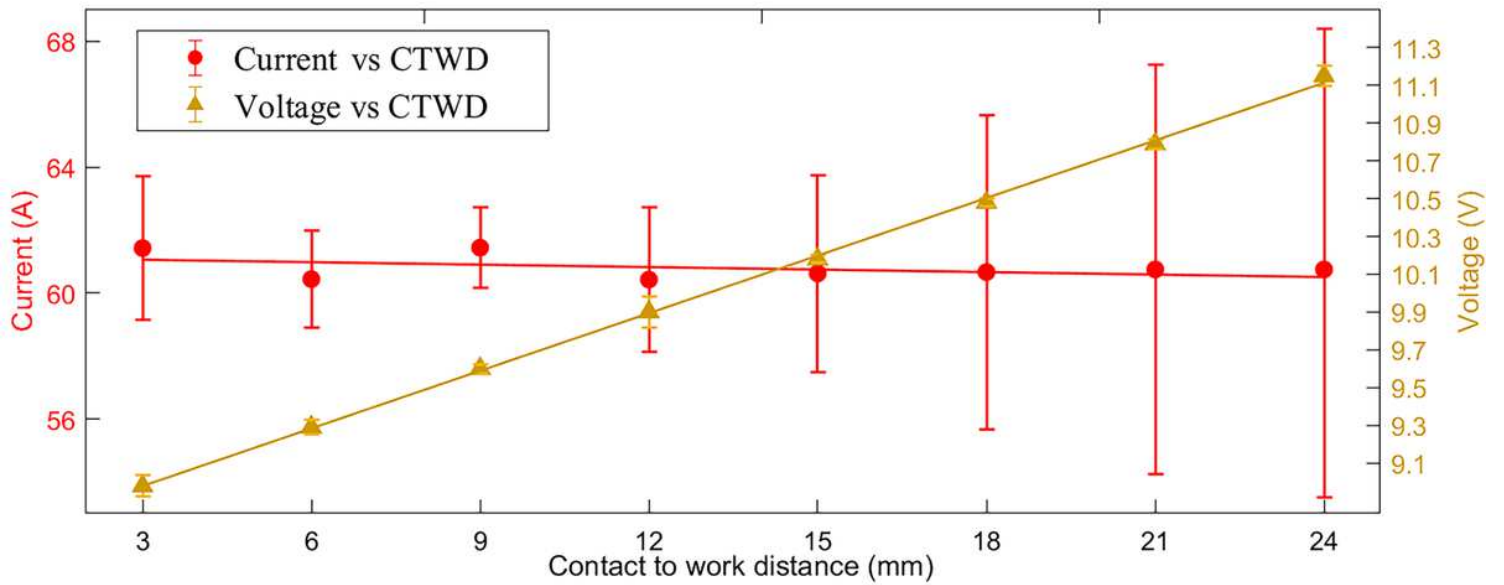


Figure 7

Changes of welding current and voltage under different CTWD, here $V_i = 0.1017c + 8.673$.

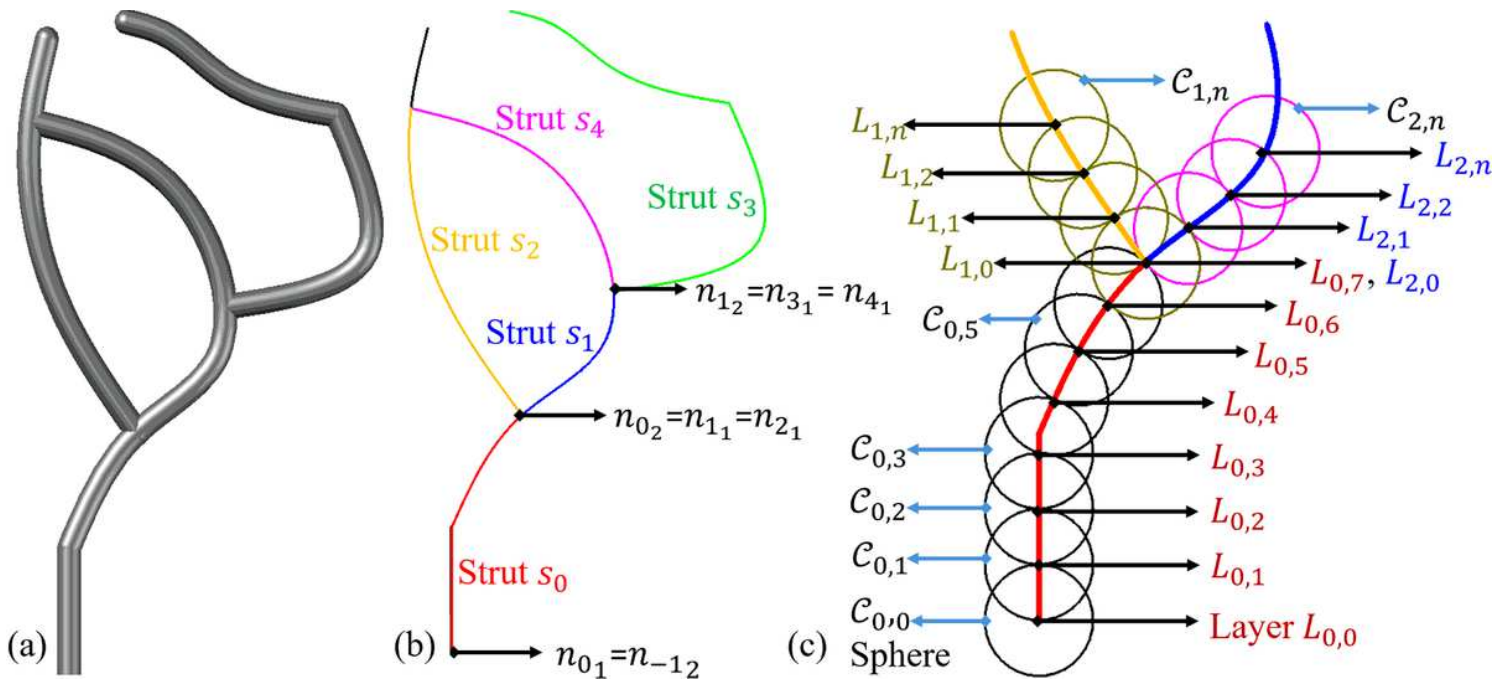


Figure 8

Schematic diagrams of slicing methods. (a) Wire structure model, (b) Acquisition of independent struts, (c) Proposed strut slicing method.

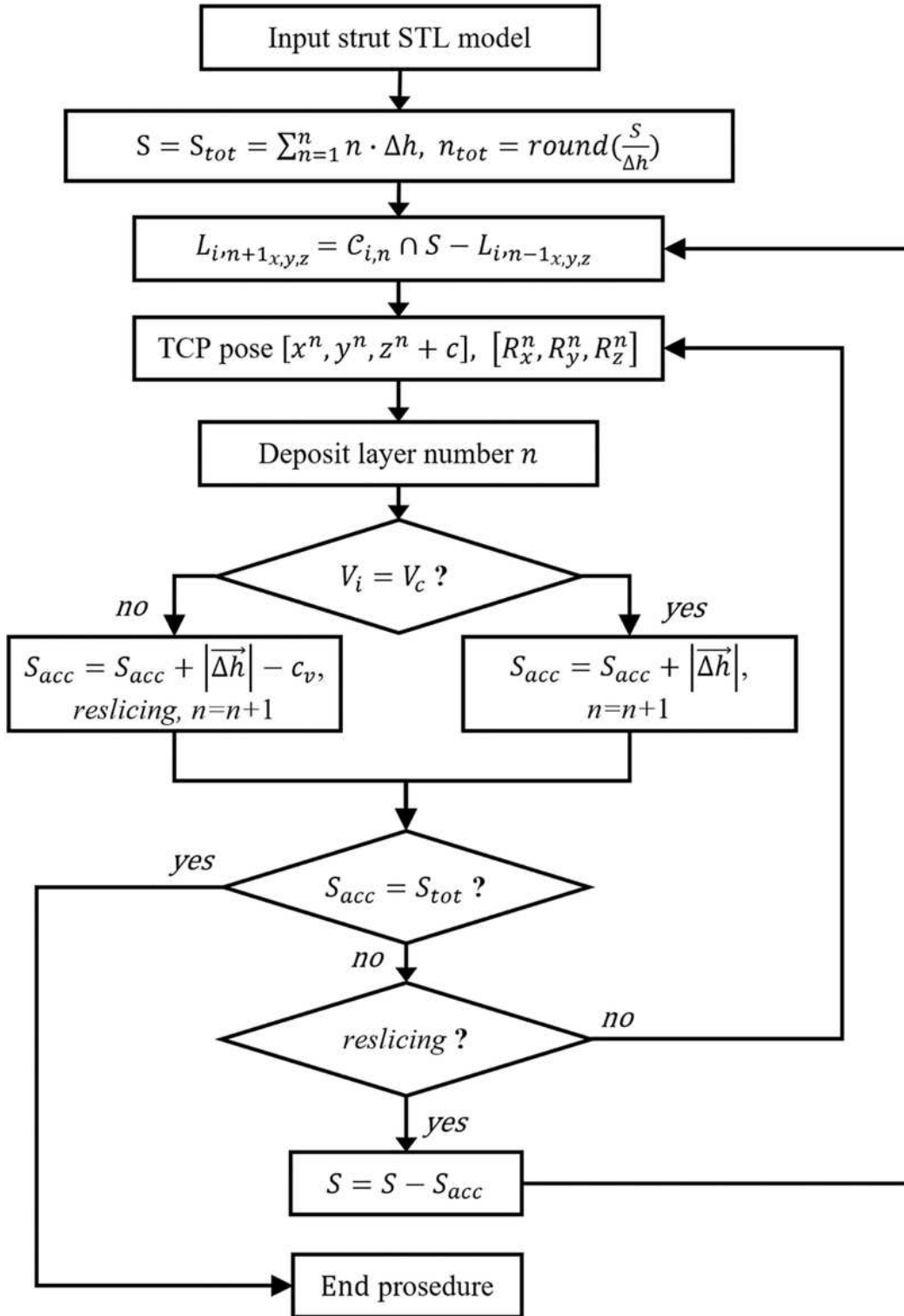


Figure 9

Processes of the slicing and height control methods for the strut.

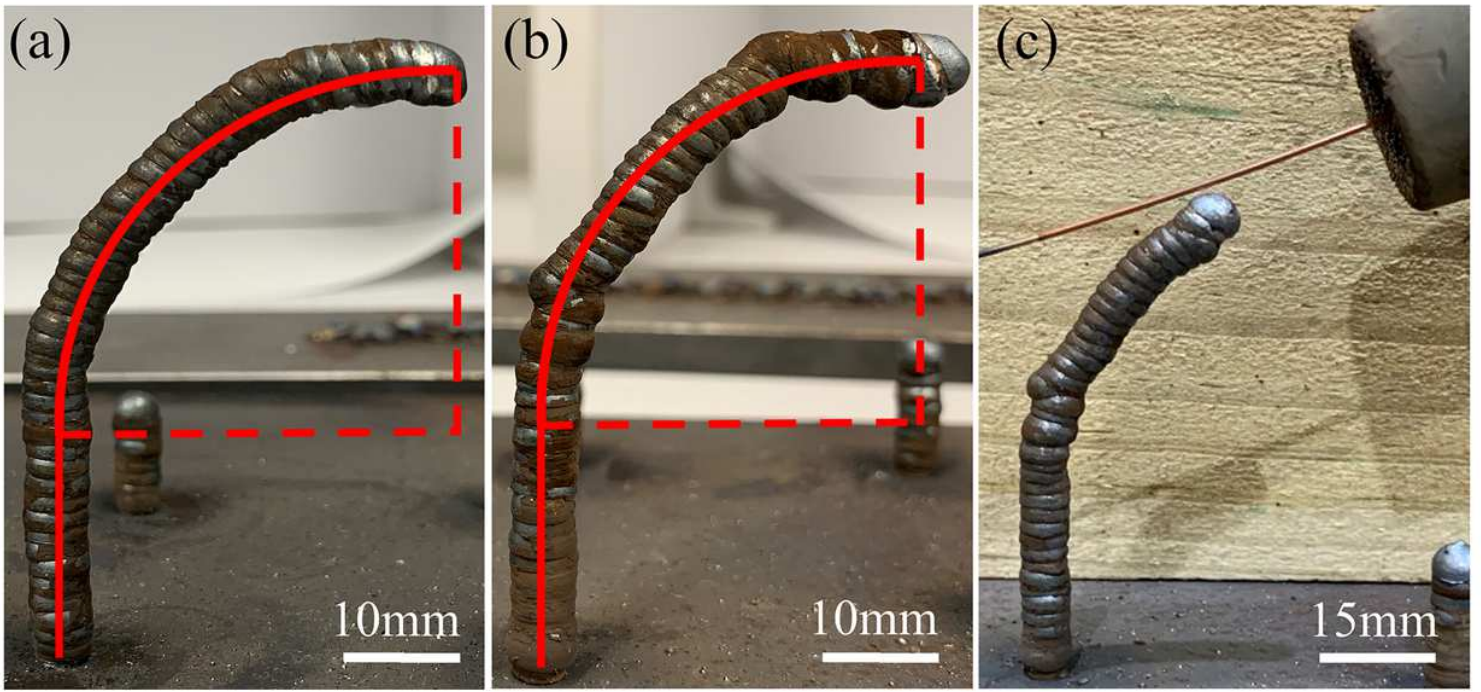


Figure 10

Arc-shaped strut deposition process (a) with adaptive CTWD changes, (b) in static deposition approach; (c) Cumulative errors in (b) discontinues the deposition.

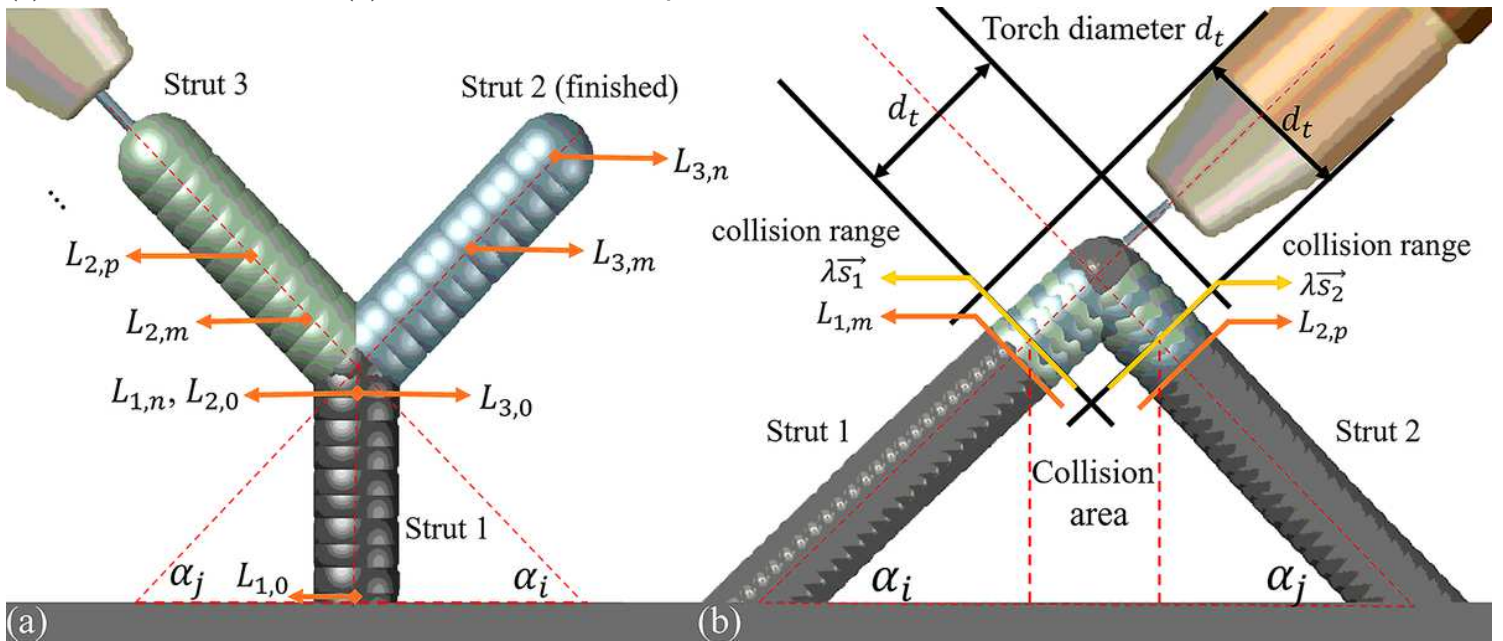


Figure 11

The example of (a) the divergence node and (b) the convergence node.

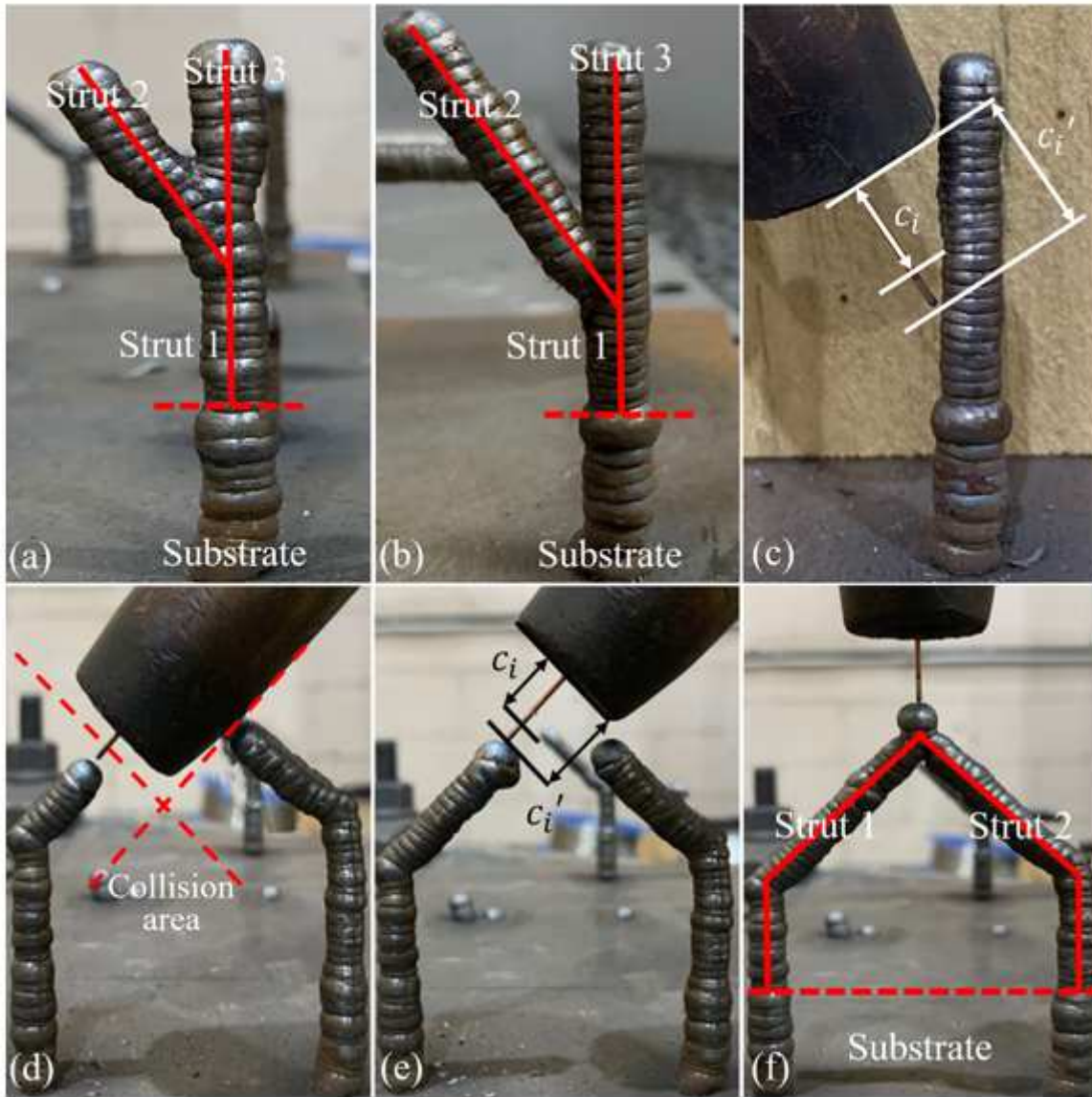
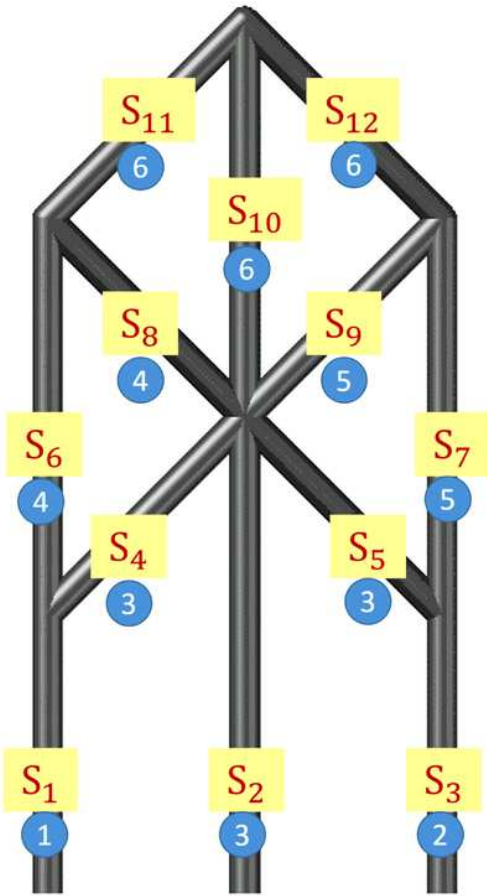


Figure 12

Examples of fabricating branch intersections. For divergence samples: (a) deposit layer-by-layer in the traditional z-direction; (b) deposit strut-by-strut in order; (c) The adaptive changes of CTWD used to avoid collisions. For convergence nodes: (d) determining the collision area (collision layer); (e) The adaptive changes of CTWD used to avoid collisions; (f) the final geometry of this sample.



- find s_1 → s_1 contact with substrate, div → deposit s_1
- find s_2 → s_2 s_4 s_5 con! → no n_{3_2} → continue
- find s_3 → s_1 contact with substrate, div → deposit s_3
- find s_4 → s_2 s_4 s_5 con! → has $n_{1_2}, n_{3_2}, n_{0_2}$ → deposit $s_{2,4,5}$
- find s_5 → finished
- find s_6 → s_6 s_8 con! → has $n_{1_2}, n_{4_2}, n_{2_2}, n_{5_2}$ → deposit $s_{6,8}$
- find s_7 → s_7 s_9 con! → has $n_{3_2}, n_{4_2}, n_{2_2}, n_{5_2}$ → deposit $s_{7,9}$
- find s_8 → finished
- find s_9 → finished
- find s_{10} → s_{10} s_{11} s_{12} con! → has $n_{6_2}, n_{8_2}, n_{4_2}, n_{5_2}, n_{2_2}, n_{9_2}, n_{7_2}$ → deposit $s_{10,11,12}$
- find s_{11} → finished
- find s_{12} → finished
- check S → \emptyset
- deposition sequence completed
- total 6 sequence

Figure 13

An example of generating a deposition sequence for a wire structure.

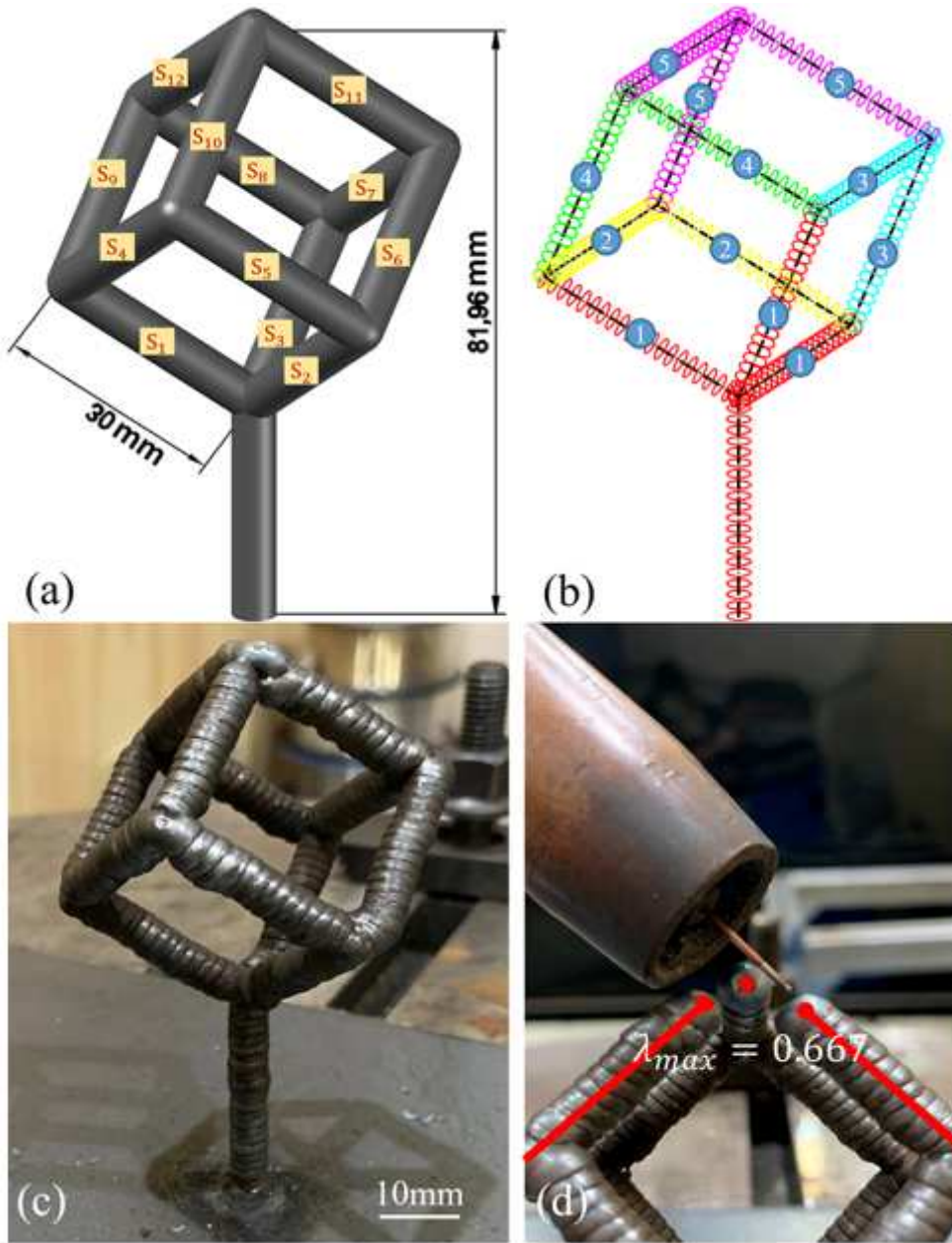


Figure 14

Cube-shaped wire structure. (a) The STL model, (b) the slicing model, (c) the final part, and (d) a fabrication detail.